

5-2016

Computational Modelling in the Development of Novel Passive Strain Sensors for Orthopedic Implants

Hunter Pelham

Clemson University, hlpelham@gmail.com

Follow this and additional works at: https://tigerprints.clemson.edu/all_theses

Recommended Citation

Pelham, Hunter, "Computational Modelling in the Development of Novel Passive Strain Sensors for Orthopedic Implants" (2016). *All Theses*. 2384.

https://tigerprints.clemson.edu/all_theses/2384

This Thesis is brought to you for free and open access by the Theses at TigerPrints. It has been accepted for inclusion in All Theses by an authorized administrator of TigerPrints. For more information, please contact kokeefe@clemson.edu.

COMPUTATIONAL MODELLING IN THE DEVELOPMENT OF NOVEL PASSIVE
STRAIN SENSORS FOR ORTHOPEDIC IMPLANTS

A Thesis
Presented to
the Graduate School of
Clemson University

In Partial Fulfillment
of the Requirements for the Degree
Master of Science
Mechanical Engineering

by
Hunter Pelham
May 2016

Accepted by:
Dr. John DesJardines, Co-Chair
Dr. Lonny Thompson, Co-Chair
Dr. Jeffrey Anker
Dr. Rodrigo Martinez-Duarte
Dr. Joshua Summers

ABSTRACT

This thesis describes the development of a series of finite element models that simulate a fractured human tibia treated with internal fixation, and a strain sensor prototype capable of objectively monitoring fracture healing with standard radiography. The models provide otherwise inaccessible insight on the mechanics of the fracture callus and fixation implant as the bone heals. Lower extremity injuries with fracture are common in the United States population with 28 million musculoskeletal injuries treated annually. Approximately two million fracture fixation surgeries are performed in the USA each year, and this is expected to exceed three million by 2025. Current clinical methods do not provide an objective measure of fracture healing or weight bearing for lower extremity fractures treated with fracture fixation. Access to the mechanical environment of bones treated with internal fixation is limited to invasive procedures where testing a variety of loading conditions is impractical. The first goal of the models is to approximate strain distributions of the internal fixation implant and the fracture callus against simulated bone healing progress. The second goal is to support the development of a passive mechanical strain sensor that is capable of monitoring bone healing through the load sharing relationship between implant and bone. The models showed rapid reductions in strain within the fracture callus, orthopedic screws and plate with increasing callus stiffness. The results also indicate significant shifts in load sharing from the implant to the healing bone between callus stiffness values of 0-10% of intact bone, when the bone begins to support the vast majority of any applied load. The computational models also confirmed orthopedic plate bending to be an effective indicator of bone healing progress. A mechanical strain sensor

was developed that is capable of monitoring orthopedic plate bending with standard radiography. The sensor uses a plate-mounted cantilevered indicator pin that spans the fracture with an internal radiopaque scale that tracks the relative motion of the pin to the plate. The sensor appropriately responded to compressive loading of the tibia in cadaveric trials and provided objective measurements of changes in plate bending with a resolution of $\sim 250\text{ }\mu\text{m}$. Finite element analysis results also predict a positive linear relationship between bone healing (percent callus stiffness) and relative pin displacement. Both the computational models and the cadaveric experiments indicate that the plate strain sensor is an effective indicator of bone healing for internal fixation applications and will provide an objective assessment of safe initiation of weight bearing.

DEDICATION

This work is dedicated to my fiancé Heather for her limitless support and to my family for a lifetime of encouragement.

ACKNOWLEDGMENTS

First, I would like to thank Dr. John Desjardins for the outstanding role he played as a mentor during my time in the Laboratory of Orthopedic Research and Design. I was fortunate to be welcomed and involved in the wonderful lab environment he has developed. I could not ask for a better advisor. I am also grateful to my fellow lab mates for the experiences that we shared. You are all awesome people. I would like to thank Dr. Jeffrey Anker for his guidance, insight, and encouragement over the course of this project. I would like to thank my co-chair, Dr. Lonny Thompson, and my committee members from Mechanical Engineering, Dr. Joshua Summers and Dr. Rodrigo Martinez-Duarte, for their feedback and advice. I would like to thank Nakul Ravikumar for his help and support when I joined the project group. I am also grateful to Melissa Rogalski and Donald Benza for all of their help and comradery both inside and outside of the lab. Finally, I would like to thank my fiancé, Heather, and my close friends, Jay and Jake for constantly providing support, humor, and general stress relief.

TABLE OF CONTENTS

	Page
TITLE PAGE	i
ABSTRACT.....	ii
DEDICATION	iv
ACKNOWLEDGMENTS	v
LIST OF TABLES	viii
LIST OF FIGURES	ix
 CHAPTER	
I. BACKGROUND	1
Bone Composition and Biomechanics	1
Physiology of Fracture Healing of Long Bones	3
Fracture Treatment Methods	4
Methods of Monitoring Fracture Healing	5
Computational Modelling for Implant Design and Fracture Healing	8
 II. ORTHOPEDIC SCREW FEA	 10
Background	10
Cannulated Orthopedic Screw Analysis	11
Methods.....	11
Results.....	14
Fixation System Analysis – Screws.....	15
Methods.....	15
Results.....	23
Discussion	27
 III. ORTHOPEDIC PLATE AND CALLUS FEA	 29
Background	29

Table of Contents (Continued)

	Page
Fixation System Analysis – Plate and Callus	30
Methods.....	31
Plate Strain Results	31
Callus Strain Results.....	39
Discussion	43
IV. DEVELOPMENT OF PLATE STRAIN SENSOR.....	48
Design Concept.....	48
Proof of Concept	49
Sensor Prototype	54
Methods.....	57
Results	60
Prototype FEA Results.....	60
Cadaver Trial Results.....	63
Discussion	65
V. CONCLUSIONS AND FUTURE WORK	68
APPENDICES	72
A: Appendix A	
Orthopedic Screw Strain – Other Loading Conditions	73
B: Appendix B	
Orthopedic Plate Strain – Other Callus Stiffness Models.....	79
REFERENCES	82

LIST OF TABLES

Table	Page
2.1 Cortical and cancellous bone material properties	18
2.2 Orthopedic screw elongation for small and large fracture gap models	23

LIST OF FIGURES

Figure	Page
1.1 External fixator rod flexion over time – Normal healing case.....	6
2.1 Cannulated orthopedic screw solid geometry created in SolidWorks	12
2.2 FEA mesh of 0.5 mm tetrahedral elements generated in Ansys v15.0.	12
2.3 Cannulated orthopedic screw boundary conditions.	12
2.4 Directional deformation (z-axis) of orthopedic screw model.	14
2.5 Small and large fracture gap geometries.....	17
2.6 Meshed geometry of internal fixation finite element model.....	17
2.7 Standing - 400 N compressive load applied to proximal fixture block	19
2.8 Coronal bending – 7,500 N·mm applied to distal fixture block	19
2.9 Coronal bending – 5,000 N·mm applied to distal fixture block.	20
2.10 Sagittal bending – 5,000 N·mm applied to distal fixture block.....	20
2.11 Axial torsion – 100 N·mm moment applied to distal fixture block.....	21
2.12 0.25 mm fracture gap model – Strain distributions of principal screw.....	24
2.13 10 mm fracture gap model – Strain distributions of principal screw.....	25
2.14 0.25 mm fracture gap model – Maximum screw strain	26
2.15 10 mm fracture gap model – Maximum screw strain.	26
3.1 No callus model – 400 N Compression – Plate center strain distribution ...	32
3.2 No callus model – 400 N Compression – Plate side strain distribution.	32
3.3 No callus model – Coronal Bending – Plate center strain distribution.....	33
3.4 No callus model – Coronal Bending – Plate side strain distribution	33

List of Figures (Continued)

Figure	Page
3.5	0.1% Callus stiffness – 400 N Compression – Center strain distribution....35
3.6	0.1% Callus stiffness – 400 N Compression – Side strain distribution35
3.7	1.0% Callus stiffness – 400 N Compression – Center strain distribution....36
3.8	1.0% Callus stiffness – 400 N Compression – Side strain distribution36
3.9	10% Callus stiffness – 400 N Compression – Center strain distribution.....37
3.10	10% Callus stiffness – 400 N Compression – Side strain distribution37
3.11	Orthopedic Plate FEA Summary – Plate Strain v/s Callus Stiffness38
3.12	0.1% Callus stiffness model – Fracture callus strain distribution.....39
3.13	1.0% Callus stiffness model – Fracture callus strain distribution.....40
3.14	10% Callus stiffness model – Fracture callus strain distribution.....40
3.15	100% Callus stiffness model – Fracture callus strain distribution.....41
3.16	Fracture Callus FEA Summary – Callus Strain v/s Callus Stiffness42
3.17	Spring model of internal fixation system.....44
3.18	Spring model – Relative displacement v/s Relative callus stiffness.....45
4.1	Plate sensor diagram – Mechanical gain = L/W48
4.2	Similar triangles that define the mechanical gain of the sensor.....49
4.3	Plate sensor – Sawbones proof of concept model.....50
4.4	X-ray images of internal scale and indicator pin51
4.5	First Cadaveric Trial – Sensor response with intact tibia52
4.6	First Cadaveric Trial – Sensor response with fractured tibia.....53

List of Figures (Continued)

Figure	Page
4.7 Strain sensor design. (A) CAD assembly of sensor system. (B) Internal scale component. (C) Exploded view	56
4.8 Cadaveric mechanical test setup with Mark-10 motorized testing stand.....	59
4.9 FEA of Sensor prototype – (A) Intact tibia strain and sensor response. (B) Fractured tibia (10 mm) strain and sensor response	60
4.10 Pin displacement and maximum callus strain v/s callus stiffness.....	61
4.11 Linear relationship between relative pin displacement and maximum callus strain	62
4.12 Second Cadaveric Trial – Sensor Response v/s Compressive Load.....	63
4.13 Radiography images of the fixation implant, fracture gap, and strain sensor for both unloaded and 100 N compression loaded cases	64
A-1 0.25 mm fracture – Screw strain distribution for 100 N·mm torsion	73
A-2 0.25 mm fracture – Screw strain distribution for sagittal bending	74
A-3 0.25 mm fracture – Screw strain distribution for coronal bending	74
A-4 10 mm fracture – Screw strain distribution for 400 N compression.....	75
A-5 10 mm fracture – Screw strain distribution for 100 N·mm torsion	75
A-6 10 mm fracture – Screw strain distribution for coronal bending	76
A-7 10 mm fracture – Screw strain distribution for sagittal bending	76
A-8 10 mm fracture – Screw strain distribution for coronal bending	77
A-9 0.25 mm fracture – Partially stripped thread – Maximum screw strain.....	77
A-10 10 mm fracture – Partially stripped thread – Maximum screw strain.....	78
B-1 5% Callus stiffness – 400 N Compression – Plate center strain distribution	79

List of Figures (Continued)

Figure		Page
B-2	5% Callus stiffness – 400 N Compression – Plate side strain distribution..	79
B-3	25% Callus stiffness – 400 N Compression – Plate center strain distribution	80
B-4	25% Callus stiffness – 400 N Compression – Plate side strain distribution	80
B-5	100% Callus stiffness – 400 N Compression – Plate center strain distribution	81
B-6	100% Callus stiffness – 400 N Compression – Plate side strain distribution	81

CHAPTER ONE

BACKGROUND

Bone Composition and Biomechanics

The mechanical properties of bone are difficult to understand due to their variability with bone type, shape, health, and the age of the individual. The bone matrix is composed of both organic and inorganic materials. The organic component of the bone matrix primarily consists of collagen and resists tensile loads, while the inorganic (mineral) component of the bone matrix provides stiffness and resistance to compression [1].

Bones can be categorized into three types based on general shape: short, flat, and long. Short bones include bones with roughly equivalent dimensions in all directions. These bones include tarsals, carpals, and vertebral bodies. Both flat and long categories describe bones with shapes that are either much larger or smaller in one dimension. Flat bones are typically thin and curved in shape. The scapula, cranial vault and the lamina of vertebrae are all examples of flat bones. Long (tubular) bones, such as femurs and tibiae, feature a thick-walled tubular diaphysis and an expanded metaphyses and epiphyses.

Bones consist of bone tissue, periosteum, and bone marrow [1]. While each of these regions have unique mechanical properties and functions, they cooperate to maintain healthy bone, repair bone fractures, and support bone growth. Bone marrow provides a source of bone cells and contains blood vessels that supply surrounding bone tissue and metabolic processes. The periosteum surrounds the surface of bones and contributes to bone blood supply. The periosteum consists of two layers: the osteogenic (inner) layer and the fibrous outer layer. The osteogenic layer houses vasculature and periosteal cells that

are capable of bone formation and resorption. The fibrous outer layer contains mostly collagen and assists in the connection between bones.

The majority of structural support comes from bone tissue. Bone tissue is divided into two forms: cortical (compact) bone and cancellous (trabecular) bone. These two forms of bone tissue have the same composition but different densities. Cortical bone surrounds cancellous bone and marrow. Cortical bone has approximately 10% porosity compared to 50-90% porosity of cancellous bone. The increased density of cortical bone allows for greater structural support since the compressive strength of bone is proportional to the square of its density. Carter and Hayers approximated the relationship between bone density and compressive strength to be:

$$S = 68\dot{\epsilon}^{0.06}\rho^2$$

where S represents compressive strength [MPa], $\dot{\epsilon}$ represents strain rate [s^{-1}], and ρ represents density [g/cm^3] [2]. However, others have found that mathematical models predicting bone strength and stiffness are only valid for the compositions used in their development. Furthermore, mathematical relationships that only consider dry density and mineral content are ineffective at predicting mechanical properties of bone [3].

Approximately 80% of the mature skeleton is comprised of cortical bone [4]. In long bones, cortical bone tissue forms the thick outer wall of the diaphysis and the thin outer walls of the metaphysis. The volume of cancellous bone increases in the metaphyses and epiphyses where the cortical tissue is thinner. The tubular structure of cortical bone tissue in long bones provides resistance to torsion and bending in the diaphysis. The high

concentration of cancellous bone in the metaphyses and epiphyses allows for more deformation and impact absorption across joints [4].

Physiology of Fracture Healing of Long Bones

Perhaps the most important aspect of bone is its ability to regenerate after fracture or other injury and restoring most or all of the form and functions of the original tissue. Facilitating bone regeneration is a key part of orthopedic treatment. Fracture healing in long bones begins with an inflammation phase where bleeding from the damaged bone forms a clot between the bone fragments. Increased cell division along the length of the bone begins between 8-24 hours after the injury within the periosteum. The periosteum provides osteoprogenitor cells. After several days, this process becomes more concentrated around the fracture site and lasts for several weeks [5]. Afterwards, fibrovascular tissue inserts collagen fibers and a matrix that will mineralize to form the woven bone tissue that makes up the fracture callus. The callus initially forms around the fracture site as both ends of the fracture are composed of dead bone tissue. Bone remodeling through bone removal and replacement by osteoclasts and osteoblasts occurs continuously throughout this process. Once the fracture gap is bridged, the remodeled bone tissue within the fracture gap can connect in a process commonly referred to as secondary bone union. Primary bone union often requires additional stability from fracture fixation treatments to be successful.

Successful bone union also depends on the type and severity of the fracture itself. Types of bone fracture can be categorized into simple, comminuted, and compound fractures. Simple fractures involve a clean break without skin penetrations. Comminuted

fractures are not clean, leaving behind bone fragments in and around the fracture site. Compound describes fractures that pierce the skin. Of these, simple fractures are the easiest to treat due to being easier to align and stabilize. Compound and comminuted fractures are more difficult to align and have a higher chance of infection. Severe fractures that are too large, not stabilized, or improperly aligned can suffer from delayed union or nonunion [6].

Fracture Treatment Methods of Long Bones

Fractures of long bones are commonly treated with immobilization, internal fixation, and external fixation. Immobilization restricts limb motion by casting or splinting to support bone healing. Typically, immobilization treatments are only viable for simple and easily aligned fractures. Internal and external fixations involves the surgical installation of orthopedic plates, screws, and rods that provide stability and alignment to the fractured limb [7]. External fixation systems extend beyond the skin from the fractured limb and are commonly required for comminuted fractures [8]. As a result, they are more prone to infection from contact with the outside. Internal fixators are the more common and preferred option due to lower infection risk. Fixation systems support any loads applied to the limb that would normally be transferred through the intact bone tissue while the fracture heals. As the fracture callus increases in stiffness in mid to late stages of bone healing, load sharing shifts from the fixation system back to the healing bone. Once the bone is fully healed, it supports all or most of any applied loads.

Internal fixators are generally composed of an orthopedic plate held against the healing bone with a set of orthopedic screws. The goal of the fixator is to provide increased

stability that will prevent micro-motion within the fracture. The fixation implant must be designed to be sufficiently stiff to provide support, but also flexible enough to not impede bone union. Installing these implants typically involves extensive surgical procedures. Implant loosening, infection, and re-fracture from early weight bearing are common modes of failure in these systems.

Internal fixation methods have evolved over time and have shifted prioritizing mechanical requirements to biological requirements [9]. Internal fixators with reduced stiffness have recently been favored to encourage callus formation. These fixators often include locking plates that are not in direct contact with the injured bone. These plates are held in an offset position with locking orthopedic screws. The extended distance from the neutral axis of the bone translates to less stiffness of the fixator. However, the increased surface area of the healing bone enhances the physiological processes and encourages secondary bone healing.

Methods of Monitoring Fracture Healing

Efforts to monitor fracture healing have typically involved advanced imaging techniques, indirect measurement through fixation performance, or a combination of both. Current clinical methods involve estimates of fracture healing through standard radiographic assessment of the fracture site. However, previous studies have shown that standard radiography does not provide an objective measure of fracture healing [10]. Song et al. found that displacement measurements using dynamic x-rays have an inter-observer variation (1.96σ) of ~ 1.5 mm, and peak variations of ~ 3.5 mm [11]. Physicians can utilize

three-dimensional CT scanning to more closely image bone density and the presence of bone union. However, CT scans are expensive and expose patients to up to 300 fold more radiation than standard X-ray imaging. Other studies have shown that radiopaque spherical beads injected into the tissue or bone surrounding the fracture can be tracked with radiostereoisometric analysis at resolutions between $\sim 20\text{-}50\text{ }\mu\text{m}$ [12]. However, this process has been impractical due to specialized training, equipment, and surgical requirements.

One measure of fracture healing and bone union is fracture stiffness [13]. Indirect measurements of fracture stiffness are possible by monitoring the mechanical response of fixation devices since load transfers from the fixator to the callus as the bone heals. Previous studies have successfully quantified bone healing patterns by monitoring strain on external fixators [14,15]. One of the sets of results from these studies is shown in Figure 1. 1.

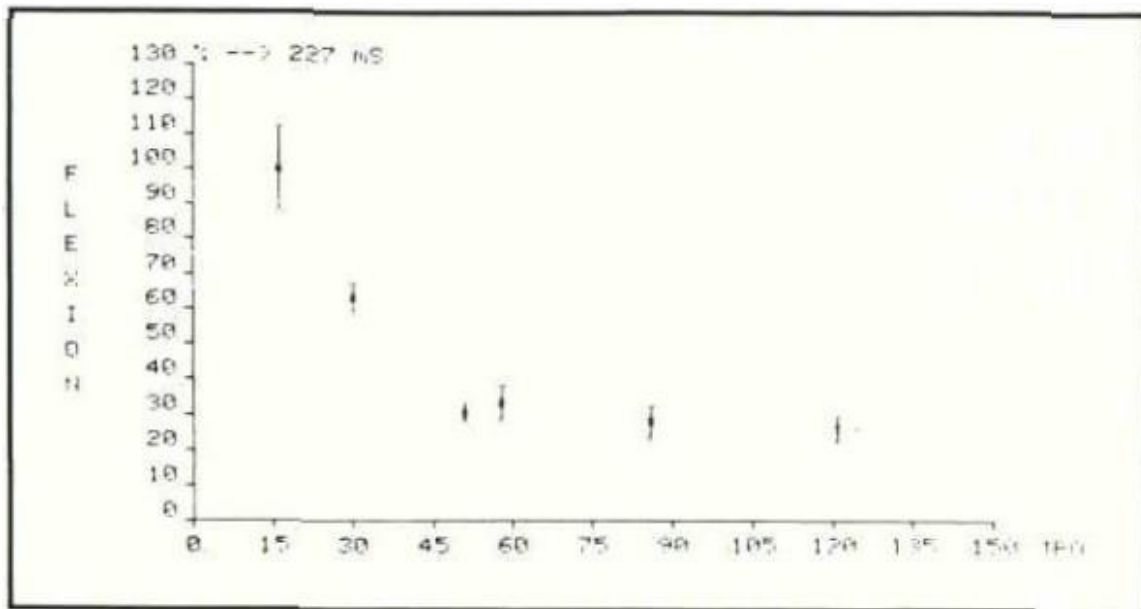


Figure 1. 1: External fixator rod flexion over time – Normal healing case

The plot in Figure 1. 1 maps the flexion of the external fixator over time as the bone heals. This particular pattern results from a normal healing case. This pattern changes if bone healing is interrupted or impaired.

Richardson et al. found that a fracture stiffness of 15 Nm/degree was an accurate threshold to indicate full weight bearing capability through indirect stiffness measurements [13]. Applying this value in clinical trials resulted in safe implant removal up to three weeks earlier than usual and a reduction in re-fracture complications from 7% (n=117) to 0% (n=95) of patients. However, these methods and improvements are limited to external fixation applications. Unfortunately, the majority of fractures are treated with internal fixation and there is no accepted method to objectively monitor bone healing non-invasively in these cases.

Another method of monitoring bone healing or implant performance *in-vivo* is through the use of “smart implants” that have some form of electronic sensor and transmission capability. However, there are some issues with supplying power to integrated sensing implants with electronics. Internal batteries are impractical due to limited battery lifetimes and limitations from biocompatibility. Direct wired systems tend to be uncomfortable to the patient and provide additional opportunities for failure. Wirelessly powered implants are widely researched, but have not been developed enough for clinical use as of yet [16].

Computational Modelling in Implant Design and Fracture Healing

Finite element analysis has been used as an alternative to invasive surgical and experimental trials to assess mechanical functionality and structures of bone tissue, fractures, and implants. Analyses of bone can incorporate computed tomography (CT) image slices to accurately represent bone structure with spatial resolutions of 250 μm . Müller and Rüegegger demonstrated that a finite element analysis using a three-dimensional stack of CT slices meshed with four-noded tetrahedron elements was effective at approximating material properties of cancellous bone [17].

Dalstra et al. described another three-dimensional finite element model that was used to simulate the mechanical response of pelvic bones and validated with cadavers fitted with strain gauges [18]. The mesh in the pelvic bone case consisted of 8-node brick elements in the trabecular and subchondral bone regions and membrane elements for the thin cortical regions. Results from the pelvic bone model overestimated stress by 10% on average in thin regions and 30% in areas of primary load transfer. They concluded that finite element models using homogenous material properties are acceptable for comparative studies, while obtaining absolute values for mechanical assessment requires more elaborate models.

Finite element analysis has also been used to optimize fracture fixation stiffness by simulating callus healing. Steiner et al. investigated fracture healing progress and outcomes in sheep tibiae against a variety of shear and axial fixation stiffness using a three-dimensional finite element model of an ovine tibia [19]. Specifically, they assessed the mechanical response of the fractured bone through the approximation of interfragmentary

motion. They predicted an axial fixation stiffness of 1000-2500 N/mm and a shear stiffness >300 N/mm optimizes bone healing in ovine long bone fractures.

Computational modeling in orthopedic applications has been a valuable tool in understanding the relationships between mechanical factors and bone healing. The insight provided by these models avoids the costly, time consuming and sometimes unavailable experimental requirements of cadaveric and animal studies. In addition, computational models offer opportunities for optimization of implant design and bone fracture treatment that were previously unavailable. As such, continuing to develop accurate simulations of structures and processes within the human body is important in ensuring efficient and effective treatment.

This thesis describes the development of a series of finite element models that simulate the mechanical response of an internal fixation system used in the treatment of a fractured human tibia. Specifically, the strain within the fracture callus, orthopedic plate, and orthopedic screws were examined. Later chapters describe the development of a plate-mounted strain sensor that responds to changes in implant strain and can be used to improve measurements taken with standard radiography.

CHAPTER TWO

ORTHOPEDIC SCREW FEA

This section describes a series of finite element analyses using Ansys v15.0 in the development of a strain indicating orthopedic screw. These models were created in parallel to the design efforts of Nakul Ravikumar in the development of a strain sensing orthopedic screw [20]. Nakul designed the screw prototypes and performed mechanical testing to evaluate their effectiveness as measurement tools. The models presented in this chapter simulated the mechanical response of orthopedic screws used in internal fracture fixation to approximate the clinically relevant range of strain in which the screw sensor should operate. The first analysis features an individual cannulated screw geometry based on the dimensions of cannulated orthopedic screws used in Instron testing of the final strain indicating screw prototype. The strain sensing orthopedic screw is capable of indicating changes in axial strain through a color change on the head of the screw. The goal of the Instron tensile testing of the screw was to validate the screw as a measurement device. The computational model of the screw was used to better understand changes in strain within the screw and to determine what the sensor is capturing.

Additional models that use the geometry of the entire internal fracture fixation system were developed to evaluate the strain response within the orthopedic screws under a variety of clinically relevant loading conditions. The magnitude, distribution, and orientation of strain within the orthopedic screws were examined. Understanding how the screws deform (elongation, bending, etc.) while supporting the healing bone was important in guiding the development of the strain sensing orthopedic screw.

Cannulated Orthopedic Screw Analysis Methods

Solid Geometry and Mesh

The goal of the individual orthopedic screw finite element model was to mimic tensile testing of the strain sensing orthopedic screw system for comparison between the computational model and experimental results. An exact geometry of the orthopedic screws was unattainable due to proprietary restrictions. As such, a solid geometry of the cannulated orthopedic screw was created in SolidWorks 2014 using measured dimensions of clinically used orthopedic screws. The primary dimensions of the orthopedic screws were a 65 mm length, a 5 mm outer diameter, a 3 mm inner (cannulated) diameter, a 7 mm major thread diameter, and a 2.5 mm thread pitch. The solid geometry and mesh of a partially threaded orthopedic screw is shown in Figure 2. 1. The mesh was generated in Ansys v15.0 using 0.5 mm tetrahedral elements. An element size of 0.5 mm was decided after a mesh convergence study revealed a percent difference of less than 1% in deformation results between 0.5 mm and 1.0 mm element sizes. The material properties of stainless steel 316L were applied to the screw geometry to match the material of the orthopedic screws used in mechanical testing.

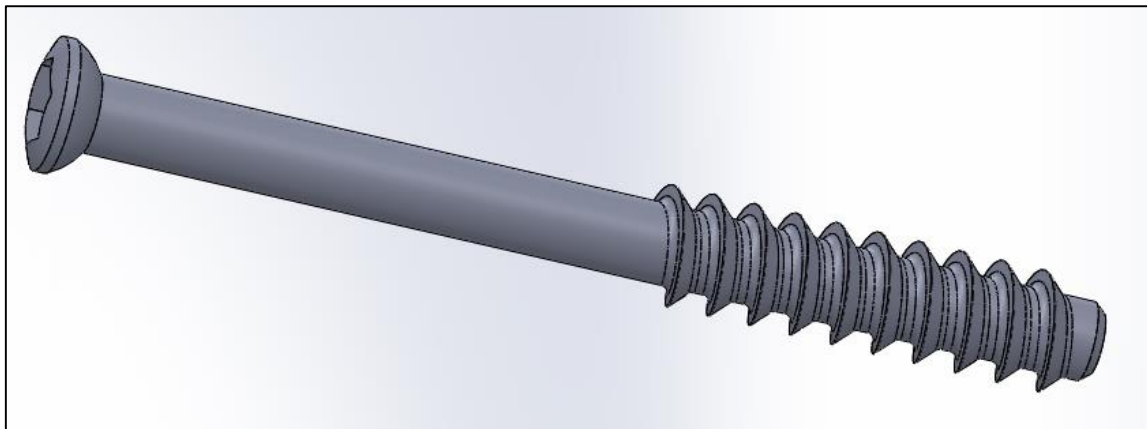


Figure 2.1: Cannulated orthopedic screw solid geometry created in SolidWorks.

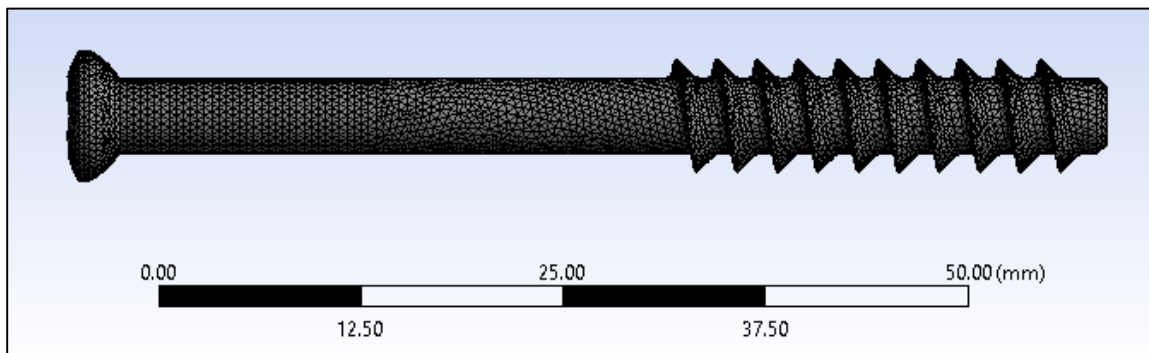


Figure 2.2: Finite element mesh of 0.5 mm tetrahedral elements generated in Ansys v15.0.

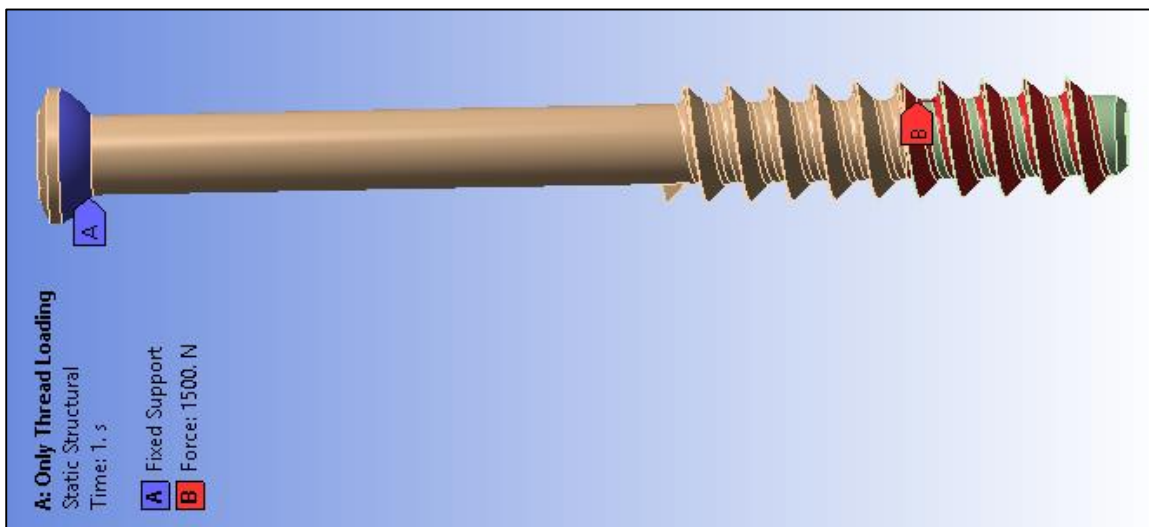


Figure 2.3: Cannulated orthopedic screw boundary conditions.

Boundary Conditions

This model is similar to the computational model presented by Nakul Ravikumar[20], but differs in where the axial loading is applied. Nakul's model applied the axial load through two points on the thread. In this model, a 1500 N tensile load is applied to five turns of the screw thread, as shown in Figure 2. 2. The model is constrained with a fixed support condition under the screw head. These conditions mirror the 1500 N tensile loading applied during experimental testing using an Instron.

Cannulated Screw Analysis Results

The estimated elongation of the orthopedic screw geometry under 1500 N axial loading is shown in Figure 2. 4 below.

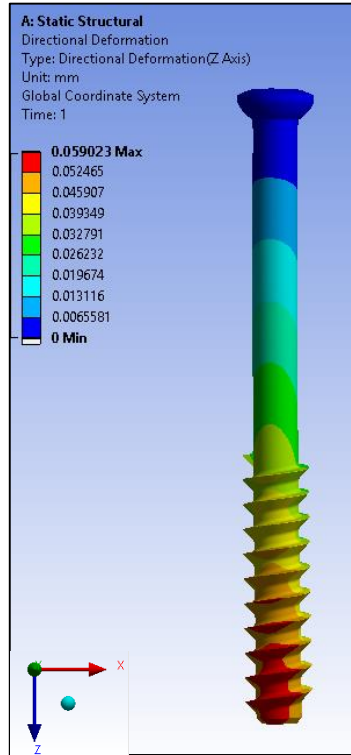


Figure 2. 4: Directional deformation (z-axis) of orthopedic screw model.

The finite element model showed a peak screw elongation of 55 μm and an average elongation of 47 μm for a 1500 N axial load. The peak elongation of 55 μm was close to the experimental elongation results of 57-59 μm with a 1500 N applied load, however the elongation on the thread end of the screw was not uniform. The average elongation of 47 μm agrees with finite element results reported by Nakul Ravikumar of 48 μm . The discrepancy between experimental results and finite element approximations exists for both computational models regardless of differences in load application.

Fixation System Analysis Methods

A fixation system finite element model was created to approximate and predict clinically relevant strain values within internal fixation implants of the human tibia. The magnitude and types of deformation these implants experience is also important. An effective measurement device design should be capable of capturing either the dominant type of deformation (elongation, bending, torsion, etc.) or a relevant combination of these. As such, an anatomic equivalent computational model capable of predicting and quantifying this information would serve as an effective design tool.

Solid Geometry and Mesh

The development of this finite element model began with the tibia geometry. An industry standard, mechanically equivalent large tibia solid geometry model (42 cm in length) was provided by Pacific Research Labs (Sawbones model #3402). This geometry included both cortical and cancellous regions of bone tissue.

A region of the tibia geometry was removed at the mid-section to represent a fracture. The size of the fracture was varied to allow for comparison between small fracture gap (0.25 mm) and large fracture gap (10 mm) scenarios, as shown in Figure 2. 5. The model assumes a clean, perpendicular fracture gap for mechanical analysis. In reality, the fracture gap is surrounded by soft tissue, bone fragments, fluid, and other physiological components. However, the material within the fracture gap in the early stages of bone healing provide an insignificant amount of mechanical support to the system. While the complexity of the fracture site (angle, number of fractures, size, etc.) does affect the

mechanical stability of the healing bone and its treatment, only a single perpendicular fracture was considered in this study.

Both ends of the tibia geometry were removed and replaced with fixture blocks orientated to establish an anatomical stance. The blocks were added to replicate common physical models used for fixturing in mechanical testing with Sawbones. An orthopedic plate CAD geometry with dimensions based on a Synthes 4.5 mm proximal tibia plate was positioned across the fracture gap and bent to match the contour of the tibia geometry. The orthopedic plate geometry includes six holes for orthopedic screws. A mesh of the internal fixation system geometry is shown in Figure 2. 6.

The fixation system geometry was meshed with tetrahedral elements of various sizes, with the exception of the fixture blocks which used mapped rectangular elements. The element sizes of the tibia/blocks, plate and screw geometries were set at 5 mm, 3 mm, and 2 mm respectively. Contact sizing of 1 mm was also applied to elements that comprise the screws and screw holes since these interfaces can cause high strain values. These element sizes were chosen after a mesh convergence study revealed a percent difference of less than 3% in strain results when reducing the element size of each component by half.

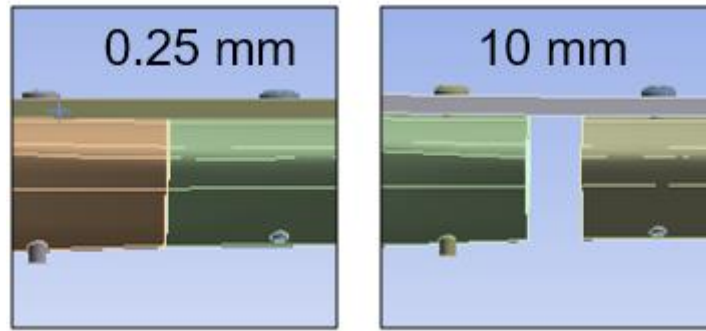


Figure 2. 5: Small and large fracture gap geometries.

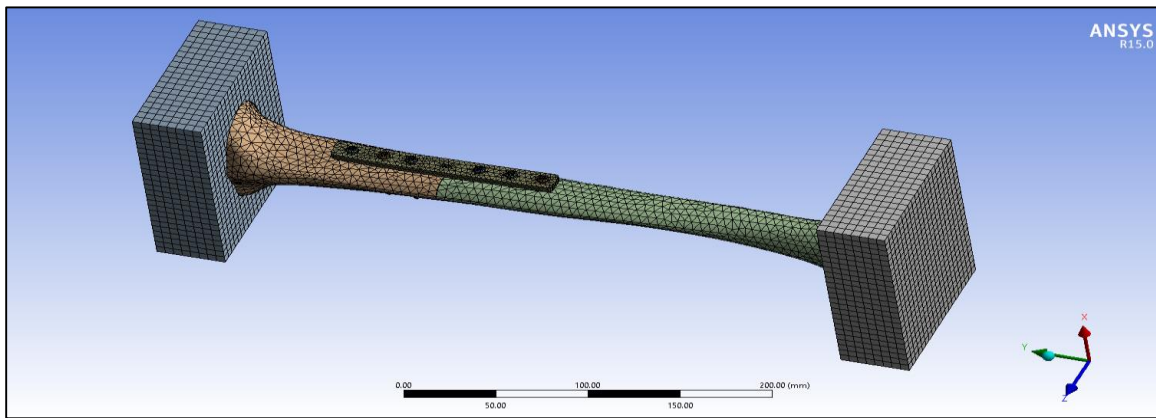


Figure 2. 6: Meshed geometry of internal fixation finite element model.

The choice for material properties used in the internal fixation model for cortical and cancellous bone was not obvious. As mentioned in Chapter 1, the mechanical properties of bone have a broad range of values based on several physiological factors including density, mineral content, bone type, and others. Initially, isotropic values for the elastic modulus and Poisson's ratio of cortical and cancellous bone were selected from ranges found in previous mechanical studies [21–23]. These initial values were set at $E_{\text{cort}} = 22 \text{ GPa}$ for cortical bone, $E_{\text{canc}} = 2.15 \text{ GPa}$ for cancellous bone, and $\nu = 0.3$ for both tissues. However, these values were replaced with anisotropic material properties provided by Pacific Research Labs. This change improved the computational model by using

industry standard properties and by making it more representative of physical models provided by Sawbones that are commonly used in mechanical testing. The anisotropic material properties are shown in Table 2. 1 taken from the Sawbones 2015 catalog.

SIMULATED CORTICAL BONE (SHORT FIBER FILLED EPOXY)				
Density	Longitudinal Tensile		Compressive	
	Strength	Modulus	Strength	Modulus
(g/cc)	(MPa)	(GPa)	(MPa)	(GPa)
1.64	106	16.0	157	16.7
Density	Transverse Tensile			
	Strength	Modulus	Note: Material property	
(g/cc)	(MPa)	(GPa)	data based on ASTM	
1.64	93	10.0	D-638 and D-695	

SIMULATED CANCELLOUS BONE (RIGID POLYURETHANE FOAM)			
	Density	Compressive	
	(g/cc)	Strength	Modulus
		(MPa)	(MPa)
Solid	0.27	6.0	155
Cellular	0.32	5.4	137
Note: Material property data based on ASTM D-1621.			

Table 2. 1: Cortical and cancellous bone material properties.

Boundary Conditions

Multiple loading conditions were applied to the fixation system analysis to better understand the mechanical performance of the orthopedic plate and screws in a variety of cases. However, some parameters remained consistent throughout all cases. First, a fixed support ($u_x, u_y, u_z = 0$) condition was applied to the proximal fixture block of the tibia geometry. Second, a pre-load of 50 N was applied to the six orthopedic screws for all cases. The remaining loads varied in magnitude and direction, but were always applied to the distal tibial fixture block opposite of the fixed support condition. The primary case of interest was that of 400 N axial compression, or half body weight, but others included coronal bending, sagittal bending, and axial torsion. These conditions are shown in Figures 2. 7 – 2. 11. Areas with applied loads are shown in red with arrows to indicate direction.

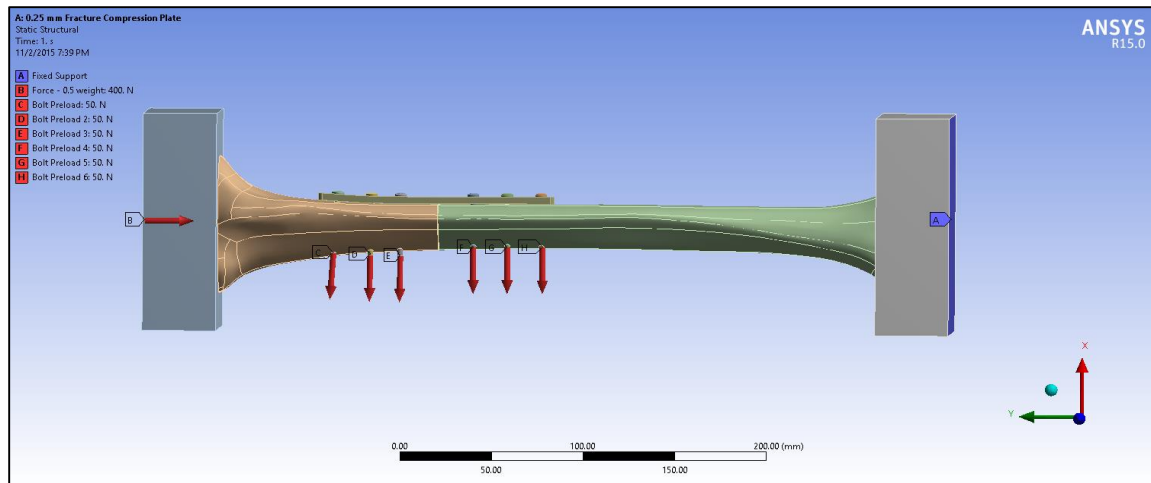


Figure 2. 7: Standing - 400 N compressive load applied to proximal fixture block.

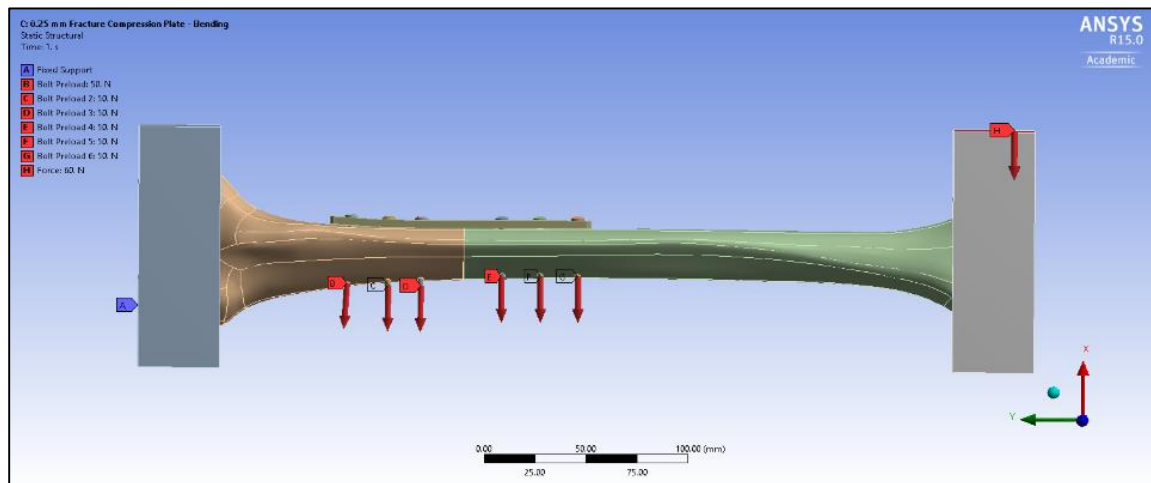


Figure 2. 8: Coronal bending (-X) – 7,500 N·mm applied to distal fixture block.

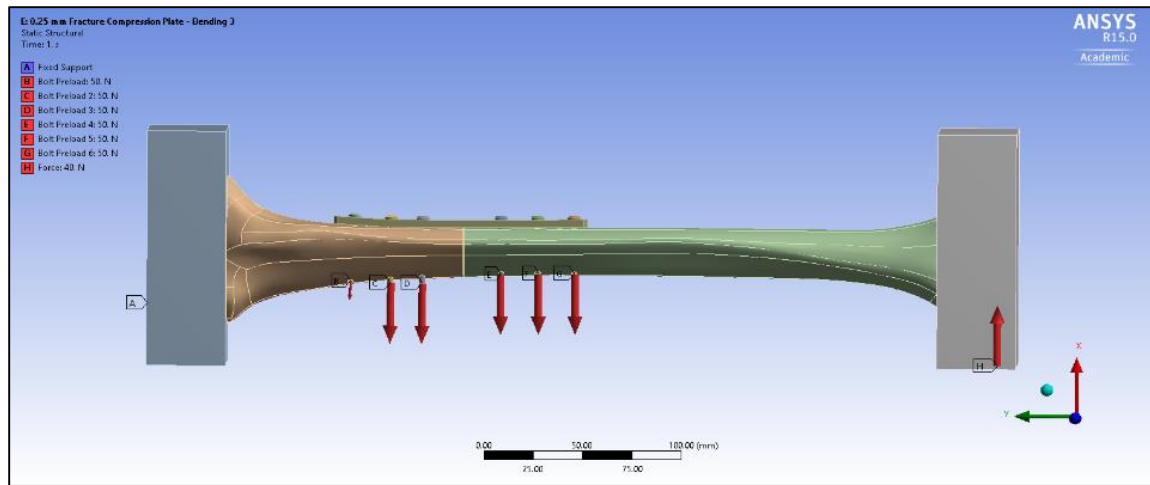


Figure 2. 9: Coronal bending (+X) – 5,000 N·mm applied to distal fixture block.

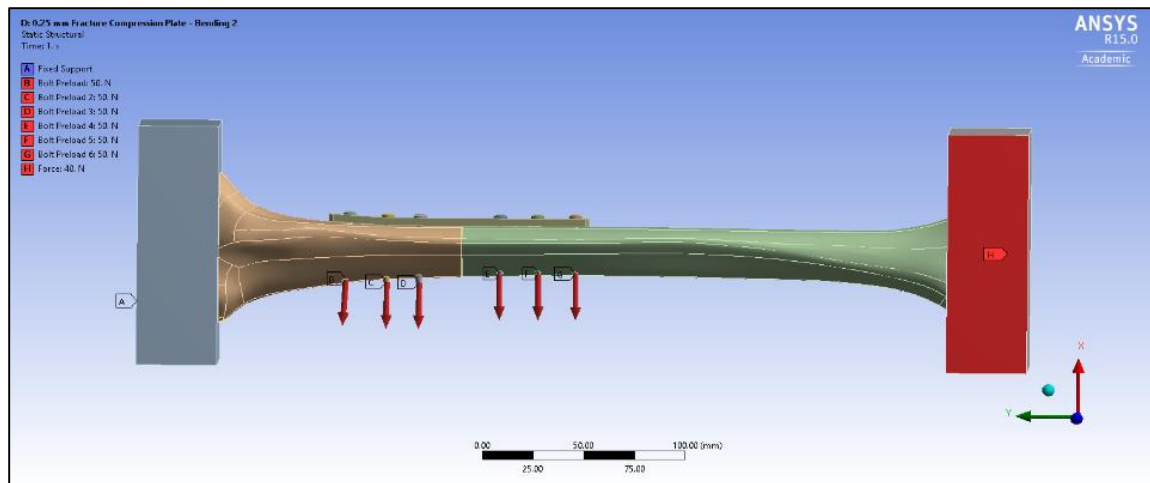


Figure 2. 10: Sagittal bending (-Z) – 5,000 N·mm applied to distal fixture block.

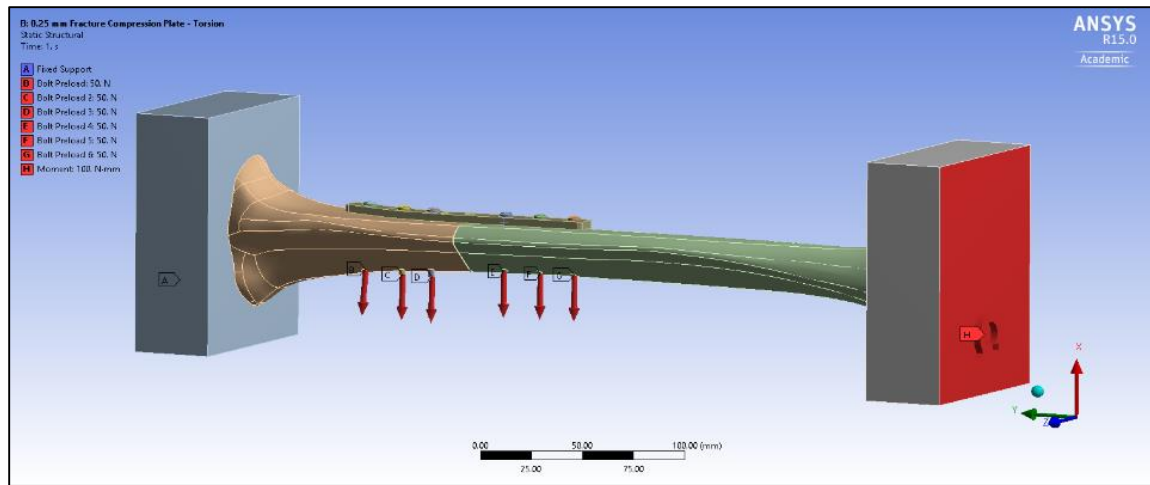


Figure 2. 11: Axial torsion – 100 N·mm moment applied to distal fixture block.

The connections between geometric bodies within the fixation model is also important, as they can drastically affect the results of the simulation. A total of 26 contact conditions were defined to realistically constrain the model. The contact conditions used include bonded, no separation, frictional, and frictionless. The orthopedic screws are in contact with the orthopedic plate with the underside of the screw heads. The screw threads are also in contact with cortical bone tissue and cancellous bone tissue. Contact between the screw heads and the orthopedic plate was defined as a “no separation” condition. Contact between the screw thread and both forms of bone tissue were defined as “bonded” to represent the interaction between the external thread of the orthopedic screws and the internal thread of the bone tissue created during implantation during surgery. A screw loosening or stripped thread scenario was also simulated by reducing the bonded contact area between the orthopedic screw threads and the bone tissue.

In reality, the orthopedic plate is compressed against the tibia by the orthopedic screws. Therefore, the contact between the orthopedic plate and the surface of the tibia could be defined as bonded or frictional depending on installation of the implant, condition of the bone, or the desired complexity of the model. This model uses a frictional contact condition with a friction coefficient of $\mu = 0.4$. This condition was chosen because it provides less stability and structural support compared to a bonded condition along the entire bottom surface of the plate, creating a more conservative approximation of mechanical response. Other contact conditions include bonded contacts between the fixture blocks and the tibia geometry, as well as a frictionless contact between the two sides of the fracture gap in the event that the fracture closes under loading.

Fixation System Analysis – Screw Results

The axial elongation of the orthopedic screws under clinical loads was found to be generally larger in the 0.25 mm fracture gap model compared to the 10 mm fracture gap model. The highest screw elongation when the tibia with a 0.25 mm fracture gap was placed under 400 N compression loading was 85 μm , compared to 54 μm screw elongation in the 10 mm fracture gap model. A summary of screw elongation results in both models under all loading conditions is shown in Table 2. 2.

Axial Elongation [mm]					
Loading Condition	Compression - 400 N	Torsion - 100 N*mm	Coronal (-X) Bending	Sagittal Bending	Coronal (+X) Bending
0.25 mm Fracture Model	0.0853	0.0927	0.1109	0.0905	0.1217
10 mm Fracture Model	0.0541	0.0641	0.0241	0.0588	0.1250

Table 2. 2: Orthopedic screw elongation for small and large fracture gap models.

A path along the longitudinal axis of each principal screw was created to generate the normal strain distribution along that axis. Strain in both axial and radial directions was examined. The strain distributions for the 400 N compression and 7,500 N·mm coronal (-X) bending cases are shown in Figures 2. 12 – 2.13. Strain distributions for the other loading conditions are shown in Appendix A. A color scale legend is shown in the left portion of each figure that maps strain values along the longitudinal axis of the orthopedic screws. The left image of each figure represents the axial strain distribution and the right image represents the radial strain distribution. A line plot of the strain values along the length of the screw is shown on the right of each image, ranging from minimum to maximum normal strain.

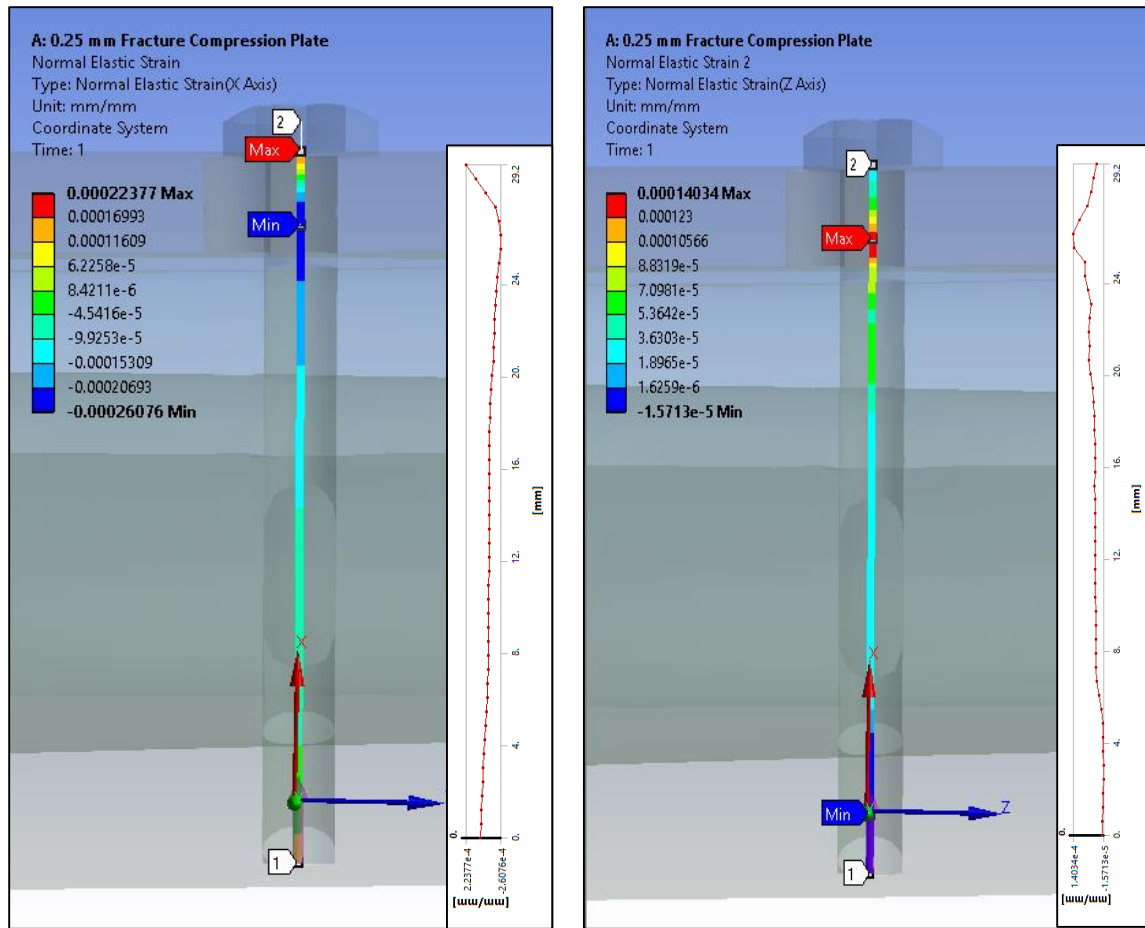


Figure 2. 12: 0.25 mm fracture gap model – Strain distributions of principal screw.

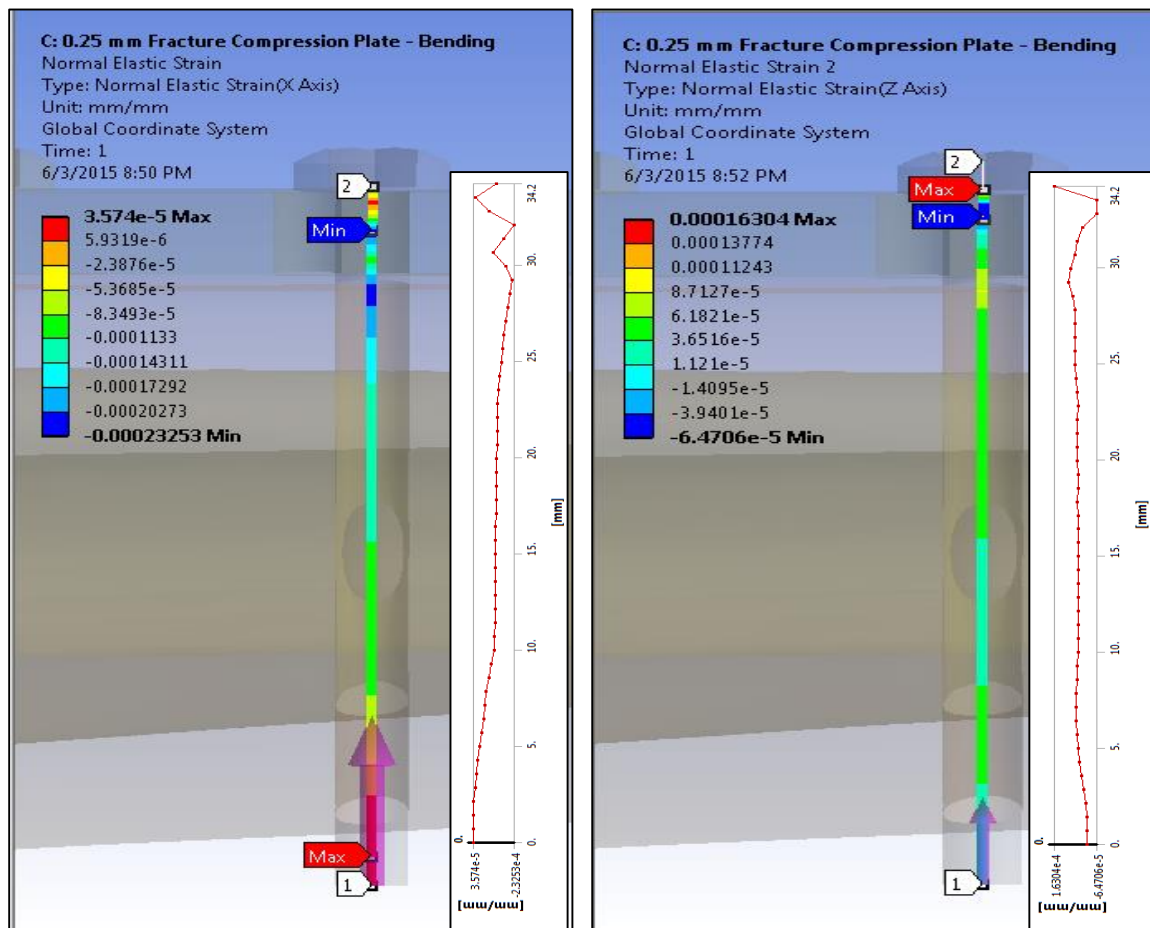


Figure 2. 13: 10 mm fracture gap model – Strain distributions of principal screw.

The maximum values of both axial and radial strain were also compared between loading conditions and fracture gap sizes. These results are shown in Figures 2. 14 – 2.15. Screw strain values for the screw loosening case are shown in Appendix A.

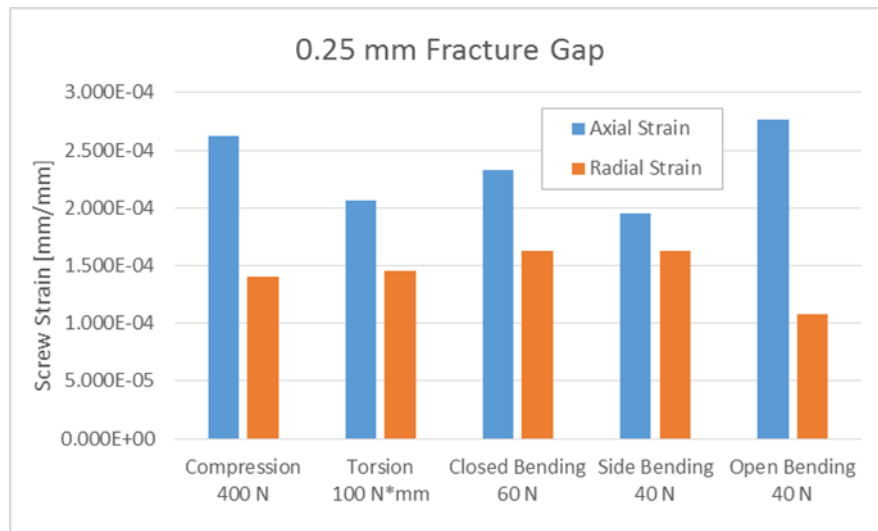


Figure 2. 14: 0.25 mm fracture gap model – Maximum screw strain.

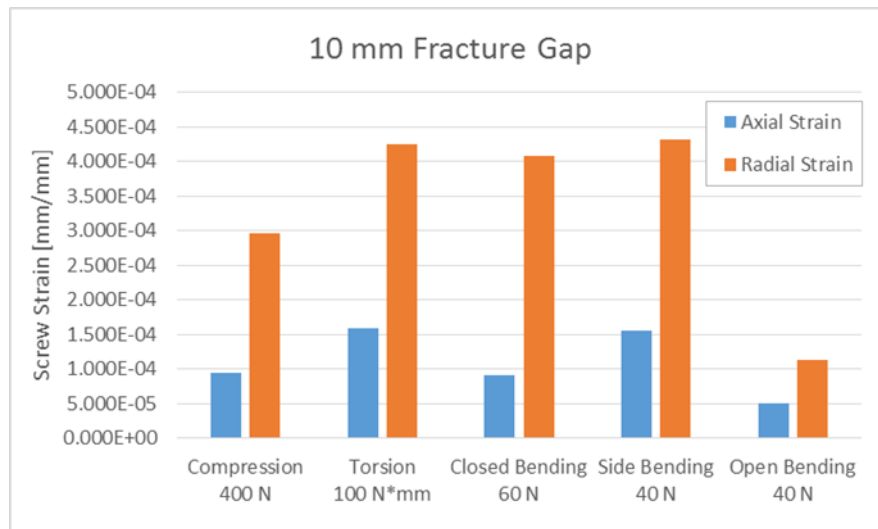


Figure 2. 15: 10 mm fracture gap model – Maximum screw strain.

The graphs show maximum normal strain of the screw on the vertical axis and the corresponding loading condition on the horizontal axis for each fracture gap model. The left data set for each loading condition represents axial strain and the right data set represents radial strain.

Discussion

The finite element model of the internal fixation system yielded several useful sets of results for each loading scenario. The first revelation from this analysis was that the screw providing the most support was always one of the two located on either side of the fracture gap regardless of loading condition. The normal strain distribution, elongation, and maximum normal strain values were examined for these principal screws in each loading case and compared.

In general, the strain distribution along the length of the screw shaft appears to be uniform for all loading conditions. However, large changes in strain magnitude and orientation occur at the interface between the tibia and the plate near the head of the screw. This area of the screw is most susceptible to bending as the screw is no longer enveloped by the bone tissue. This is reflected in the results of the finite element model for both small and large fracture gaps.

Determining the composition of normal strain within the orthopedic screw is important in developing a strain sensing screw since initial designs only respond to axial elongation of the screw. The maximum strain results of the finite element models show a combination of both axial and radial strain along the length of the orthopedic screws. They

show a dominance of axial screw strain for all applied loading conditions when the fracture gap is small (0.25 mm). However, when the fracture gap is large (10 mm) the dominant orientation of screw strain is radial for all applied loading conditions.

Screw elongation results reflect this trend as well. The 0.25 mm fracture gap model approximates higher screw elongation values compared to the 10 mm fracture gap model for all loading conditions with the exception of the coronal (+X) bending case. These results indicate that both elongation and bending are relevant forms of screw deformation under clinical loads. Therefore, a strain sensing screw design capable of detecting both screw bending and elongation would be the most effective at monitoring implant loads. A combination of a screw that responds to elongation and a screw that responds to bending within the same internal fixation system could be an alternative solution instead of a single multi-functioning screw design.

CHAPTER THREE

ORTHOPEDIC PLATE AND CALLUS FEA

One measure of fracture healing and bone union is fracture stiffness [13]. Indirect measurements of fracture stiffness are possible by monitoring the mechanical response of fixation devices since load transfers from the fixator to the callus as the bone heals. Previous studies have successfully quantified bone healing patterns by monitoring strain on external fixators [14,15]. Unfortunately, the majority of fractures are treated with internal fixation and there is no accepted method to objectively monitor bone healing non-invasively in these cases. As a result, there is little information regarding the mechanical response of internal fixation systems during fracture healing. Understanding strain within the fracture callus itself during this process is beneficial in preventing re-fracture from early weight bearing or lost productivity from delayed weight bearing.

The internal fixation system finite element model described in Chapter 2 was built upon to quantify changes in load sharing between the implants and the bone as the fracture callus heals and increases in stiffness. Prior studies have shown that as fracture calluses mature during early healing, their stiffness exponentially increases from a Young's modulus of $\sim 5 \times 10^4$ Pa for granulation tissue to $\sim 2 \times 10^{10}$ Pa for mature cortical bone, and the ultimate strength of the callus also increases at approximately half the rate of the stiffness [24,25]. The primary goal of this analysis was to identify ranges of callus stiffness and implant strain that correspond with when the patient is safe for weight bearing after surgery.

Methods

Solid Geometry and Mesh

The geometry of this orthopedic plate analysis is based on the solid geometry from the internal fixation system model described in chapter 2. However, only the large fracture gap (10 mm) model was considered in this analysis since large fractures of the tibia are more severe and more commonly treated with internal fixation. In the original model, a section of the tibia geometry was removed to create the fracture. This section was added back to the model to represent the fracture callus that forms as the bone heals and bridges the fracture gap with new tissue.

Adjusting the material properties of the fracture callus geometry allows the model to simulate the performance of the fixation system and the tibia at various stages of bone healing. Specifically, the Young's modulus of the fracture callus geometry was varied between 0.01% - 100% of the modulus for intact bone. The orthopedic plate geometry and screws were also removed in a set of cases to better understand the impact of the internal fixation system on load sharing with the bone tissue with variable callus stiffness. This was a hypothetical case for comparison of equivalent strain within the fracture callus with and without fixation since bone union of a large fracture is unlikely without the added stability of fixation implants. The mesh is composed of tetrahedral elements with an element size of 2 mm for the screws, 3 mm for the orthopedic plate, and 5 mm for the tibia geometry, fracture callus, and fixture blocks.

Boundary Conditions

The fracture callus model uses the compression and coronal bending loading conditions described in the fixation system model. In the compression case, a 400 N (half body weight) is applied to the proximal fixture block while the distal fixture block is fully constrained to simulate standing. In the coronal bending case, the proximal fixture block is fixed while a 60 N load is applied to the distal fixture block. Bonded contact conditions were added to the elements in the regions between the fracture callus and the tibia geometry. Other contact conditions remained unchanged.

Results

Orthopedic Plate Strain

Equivalent strain distribution results along the length of the orthopedic plate revealed the majority of strain to be either directly above or near the fracture site. This result was expected as the fracture site creates a fulcrum that encourages bending within the plate under the compression and coronal bending loading conditions. The equivalent strain distribution along the center and side of the orthopedic plate under both loading conditions without the fracture callus is shown in Figures 3.1 – 3.4. Line plots of the strain along the length of the plate are shown as well. The vertical axis of the line plots range from the minimum to the maximum equivalent strain of the plate for each loading condition.

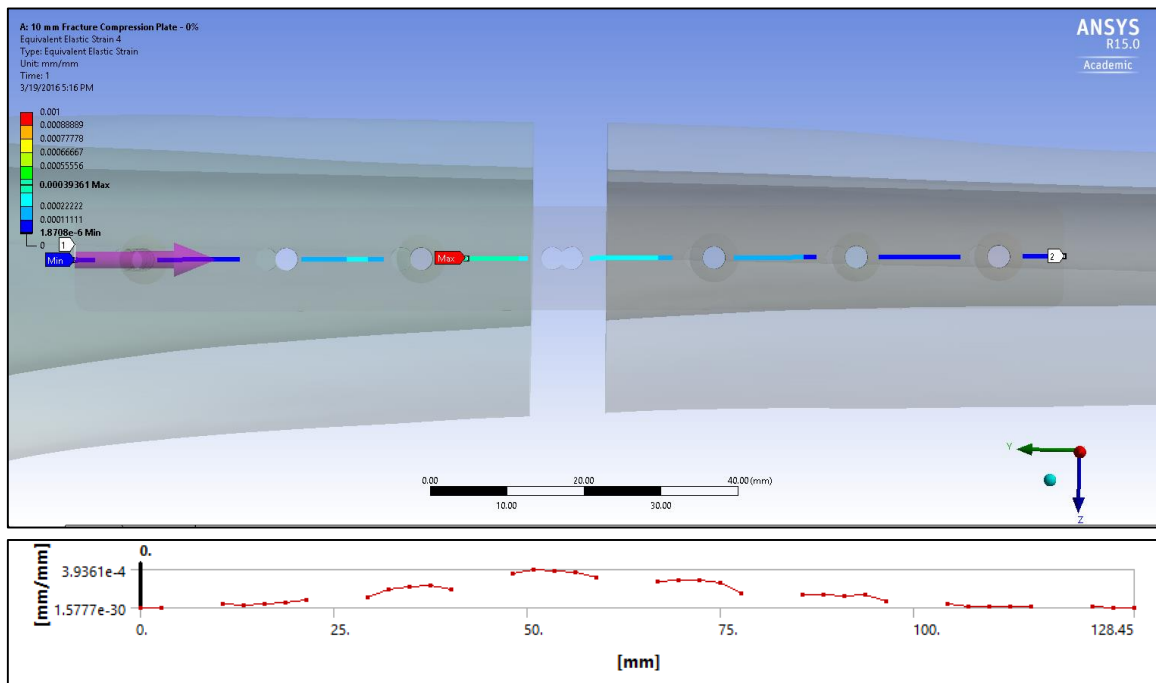


Figure 3. 1: No callus model – 400 N Compression – Plate center strain distribution.

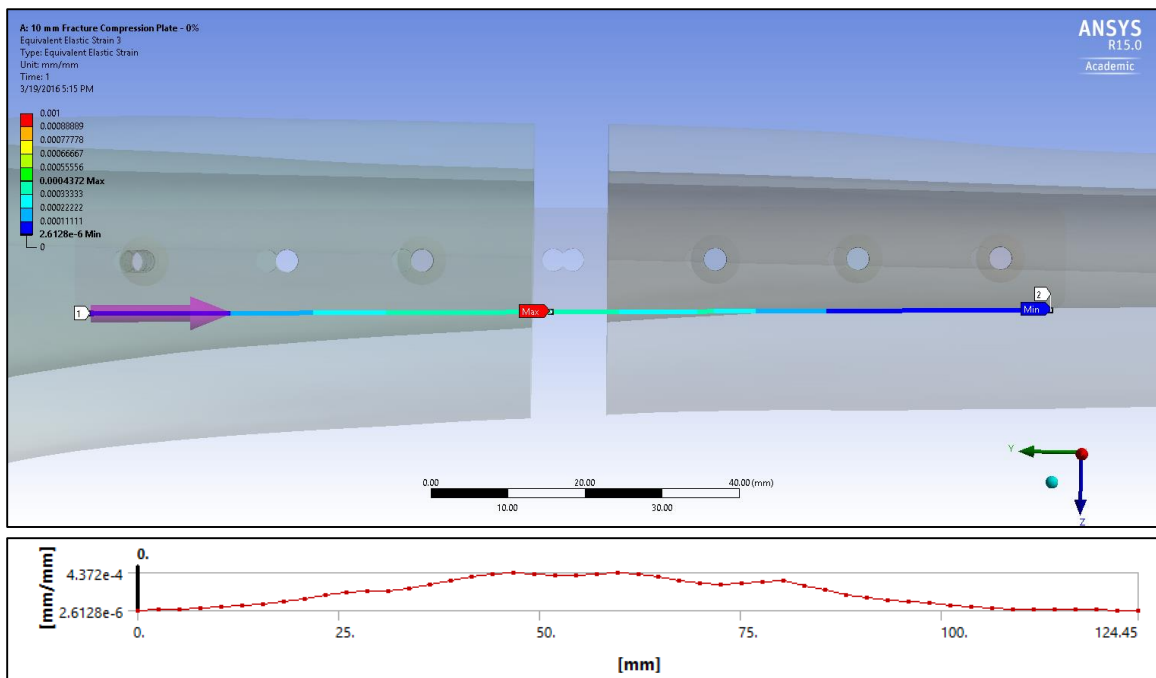


Figure 3. 2: No callus model – 400 N Compression – Plate side strain distribution.

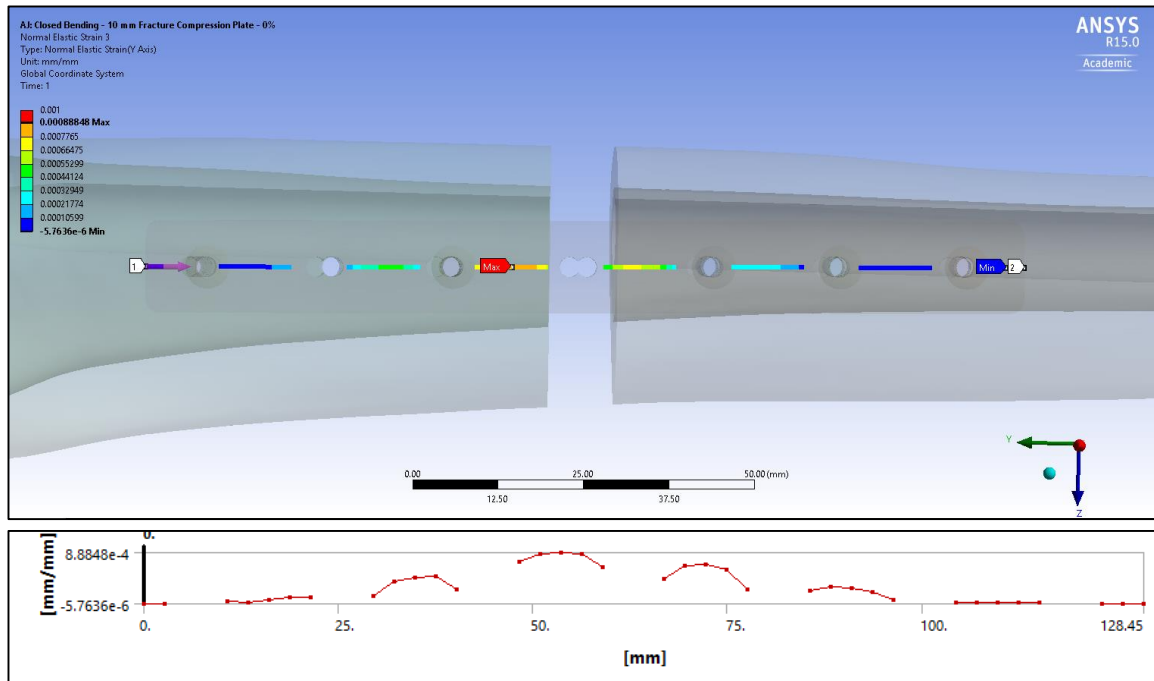


Figure 3. 3: No callus model – 7,500 N·mm coronal (-X) bending – Plate center strain distribution.

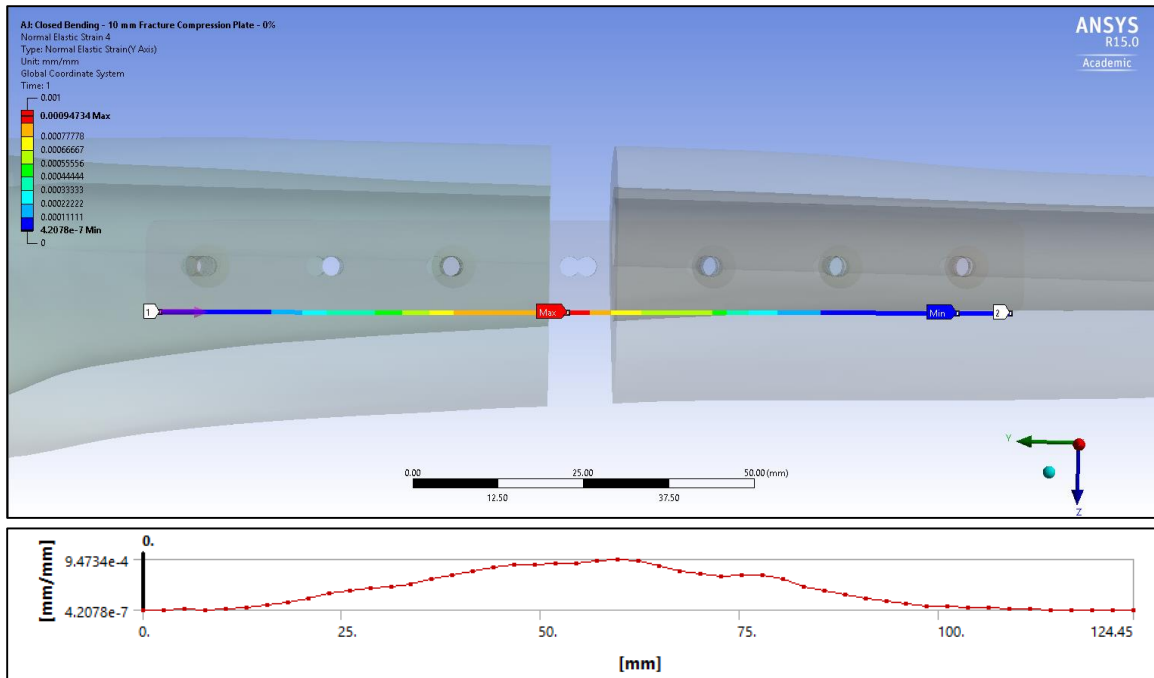


Figure 3. 4: No callus model – 5,000 N·mm coronal (+X) bending – Plate side strain distribution.

The computational model also showed a significant reduction in equivalent strain within the orthopedic plate as the fracture callus stiffness was increased. The strain distributions within the plate from the 0.1%, 1%, and 10% callus stiffness models are shown in Figures 3. 5 – 3. 10. Results from other models with callus stiffness varying from 0.1% - 100% of intact bone stiffness are shown in Appendix B.

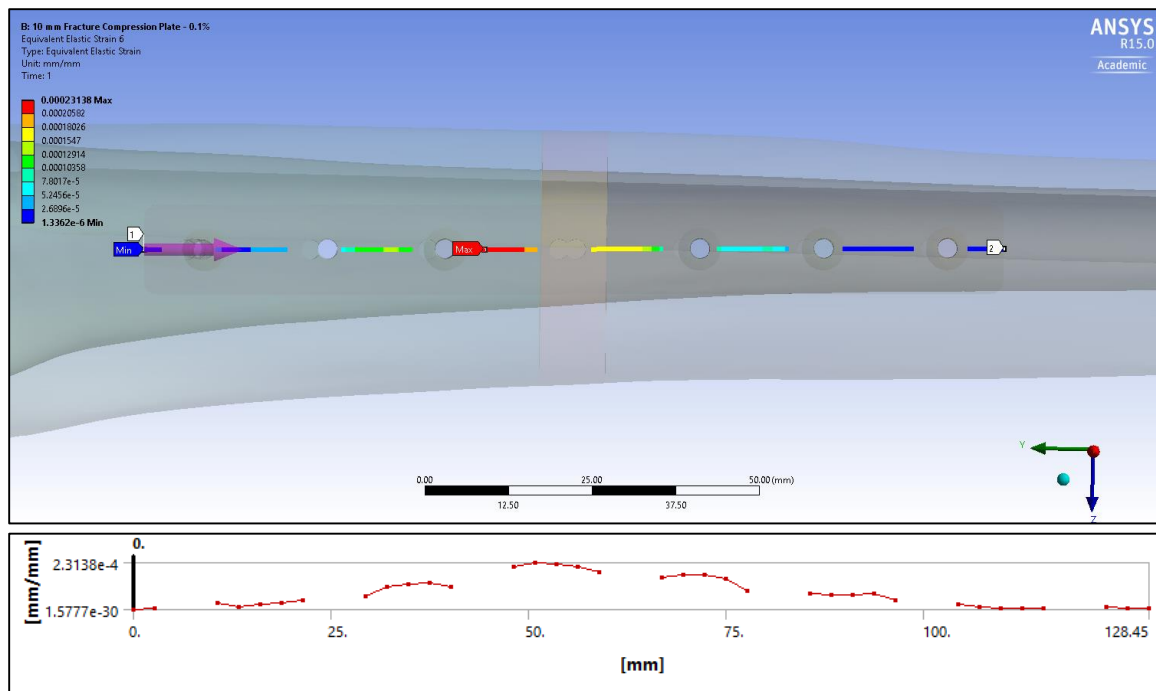


Figure 3. 5: 0.1% Callus stiffness – 400 N Compression – Plate center strain distribution.

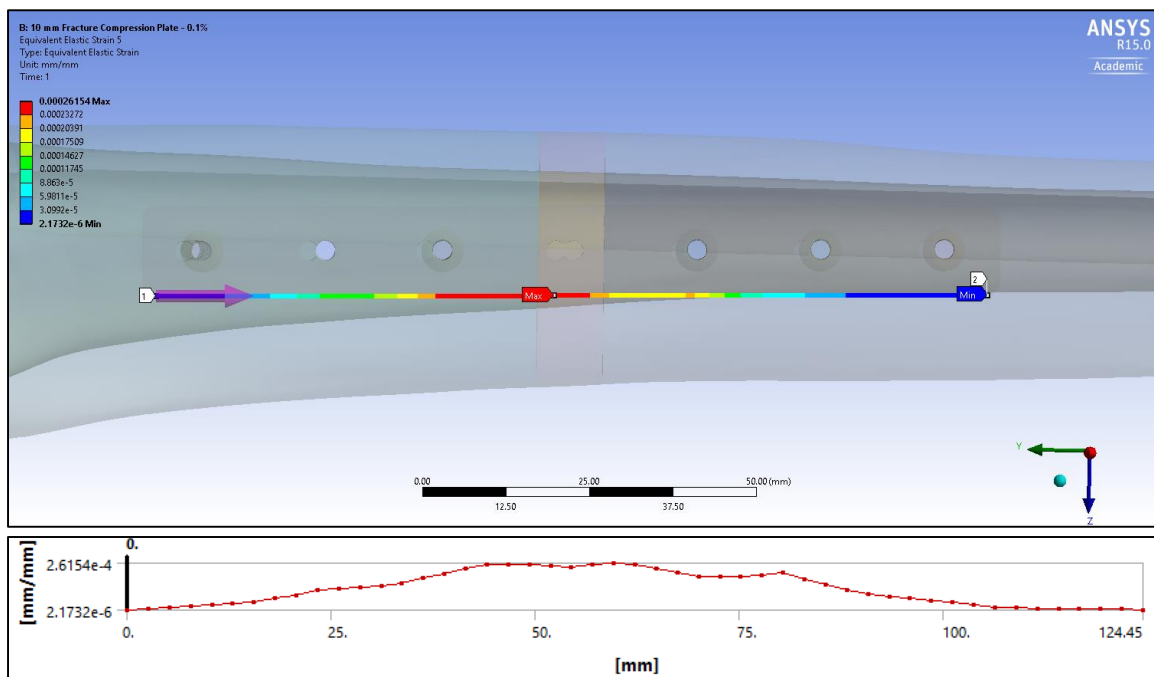


Figure 3. 6: 0.1% Callus stiffness – 400 N Compression – Plate side strain distribution.

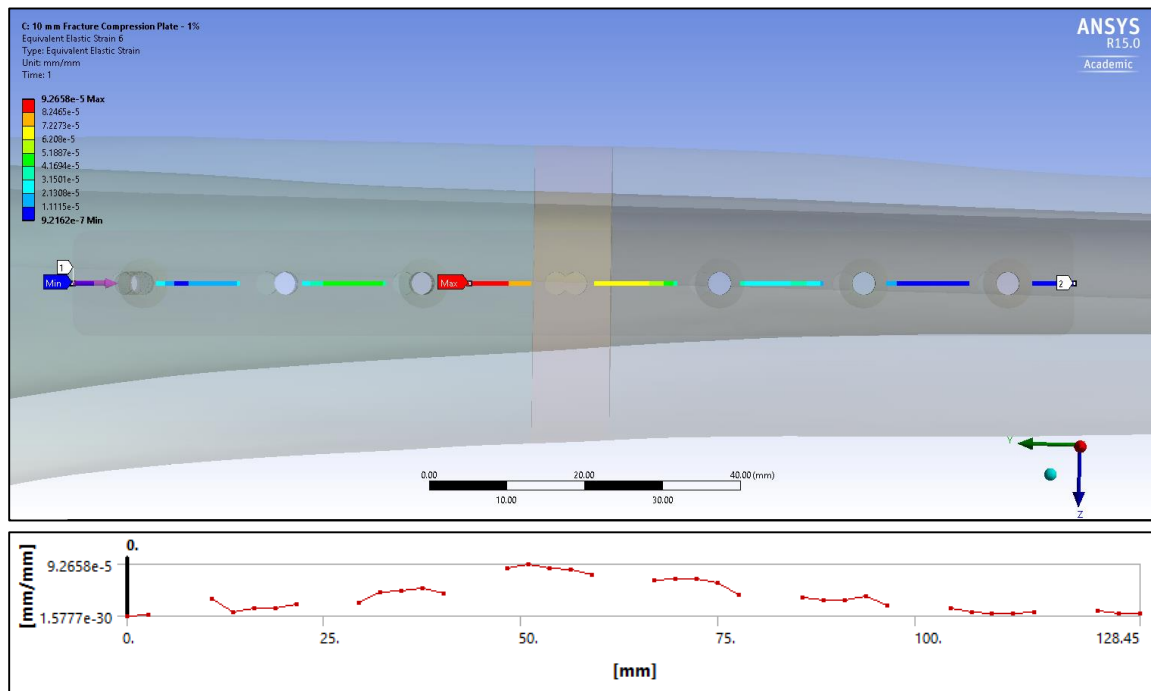


Figure 3. 7: 1.0% Callus stiffness – 400 N Compression – Plate center strain distribution.

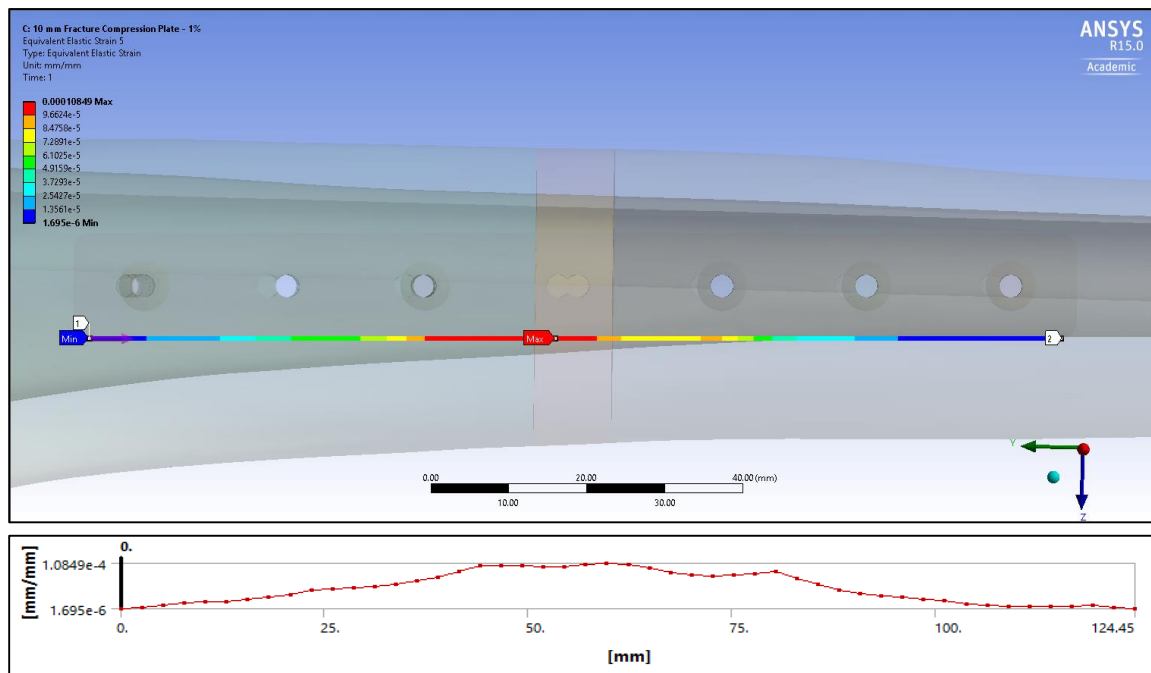


Figure 3. 8: 1.0% Callus stiffness – 400 N Compression – Plate side strain distribution.

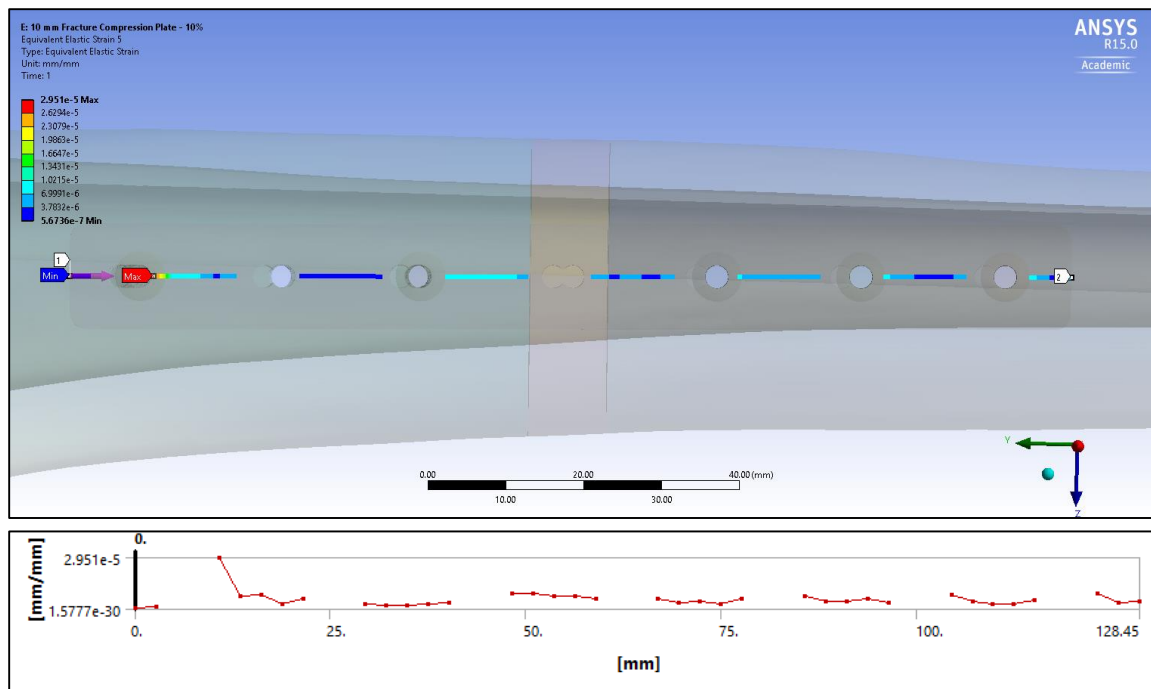


Figure 3. 9: 10% Callus stiffness – 400 N Compression – Plate center strain distribution.

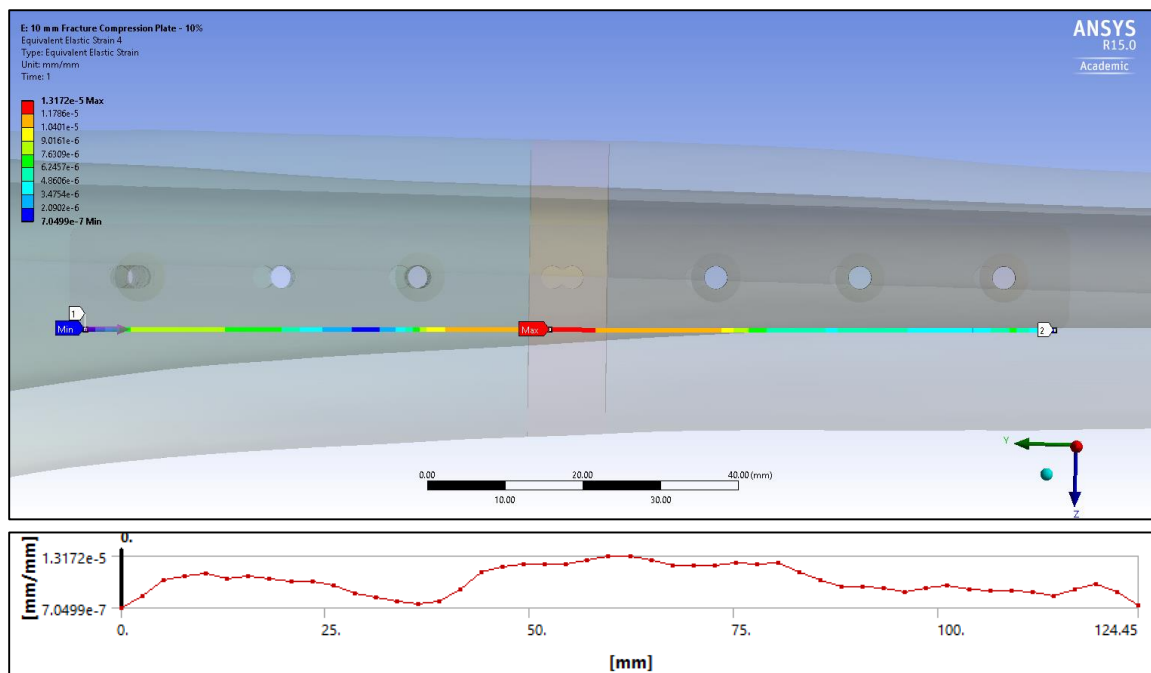


Figure 3. 10: 10% Callus stiffness – 400 N Compression – Plate side strain distribution.

A summary of the equivalent strain results of the plate from the fracture callus models are shown in Figure 3. 11.

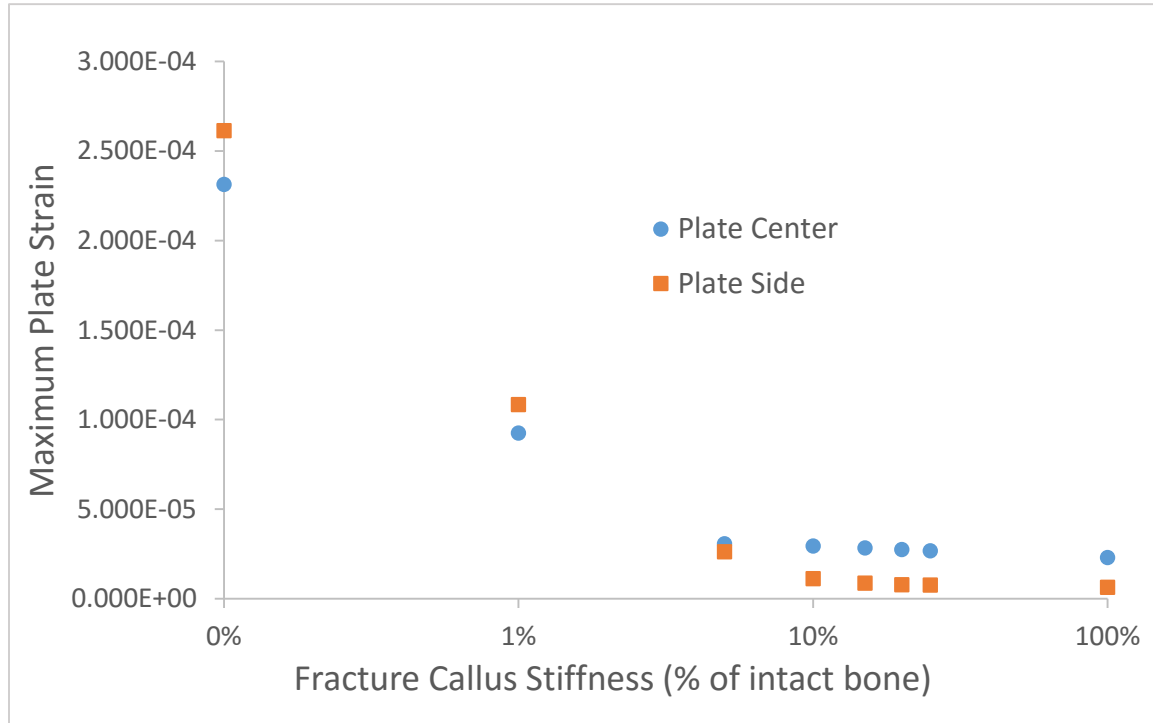
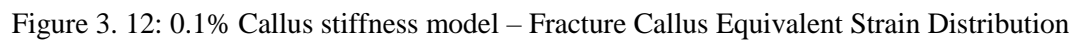


Figure 3. 11: Orthopedic Plate FEA Summary – Plate Strain v/s Callus Stiffness

Figure 3. 11. Shows maximum equivalent strain of the plate on the vertical axis and fracture callus stiffness on the horizontal axis with a logarithmic scale. According to the finite element models, maximum plate strain decreased rapidly as fracture callus stiffness increases from 0% - 100% of intact bone. The highest strain value of 3.936×10^{-4} within the plate occurred in the model without a callus geometry (0% stiffness). Strain within the orthopedic plate continued to decrease with callus stiffness before plateauing at a strain value of 6.348×10^{-6} between 5-10% callus stiffness. The equivalent strain results along both the center and side of the plate followed this trend.

Strain within the fracture callus was approximated for comparison with plate strain as callus stiffness increased. Callus strain in tibia models without fixation implants were also examined. The strain distributions of the fracture callus geometry are shown in Figures 3. 12 – 3. 15 for callus stiffness values of 0.1%, 1%, 10% and 100% of intact bone. Note that the distribution results are shown with a logarithmic scale.



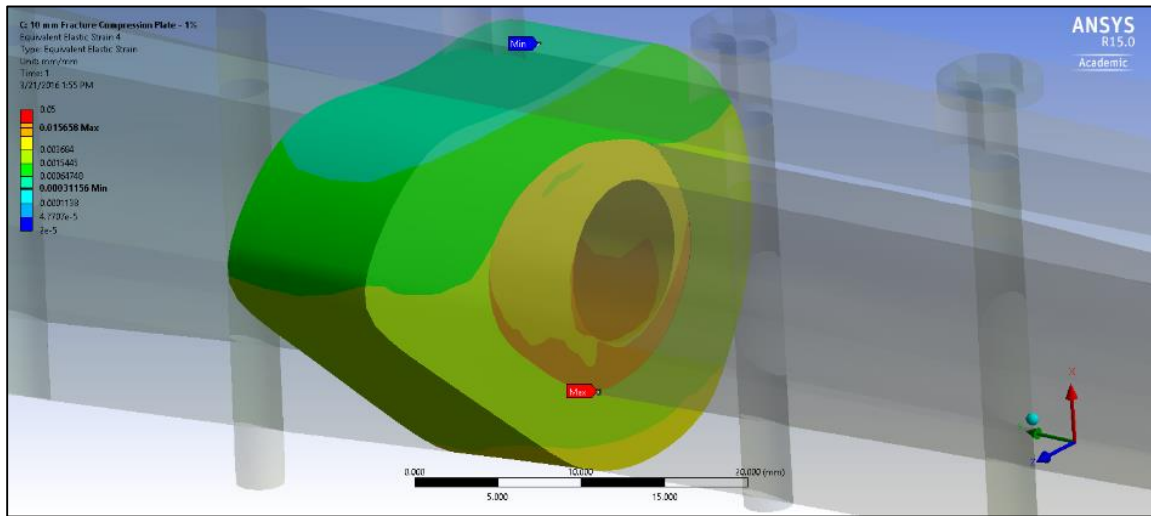


Figure 3. 13: 1.0% Callus stiffness model – Fracture Callus Equivalent Strain Distribution

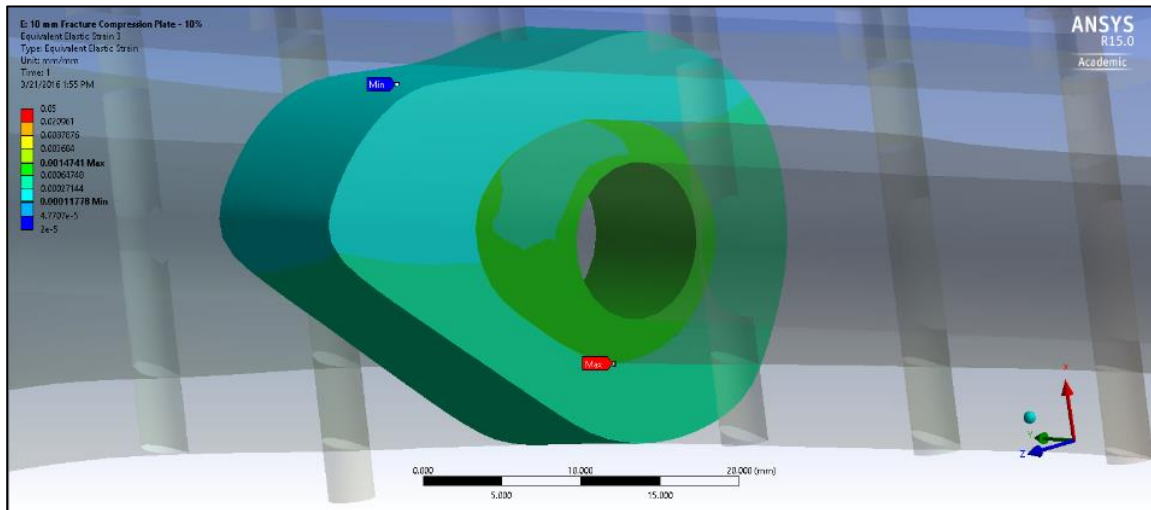


Figure 3. 14: 10% Callus stiffness model – Fracture Callus Equivalent Strain Distribution

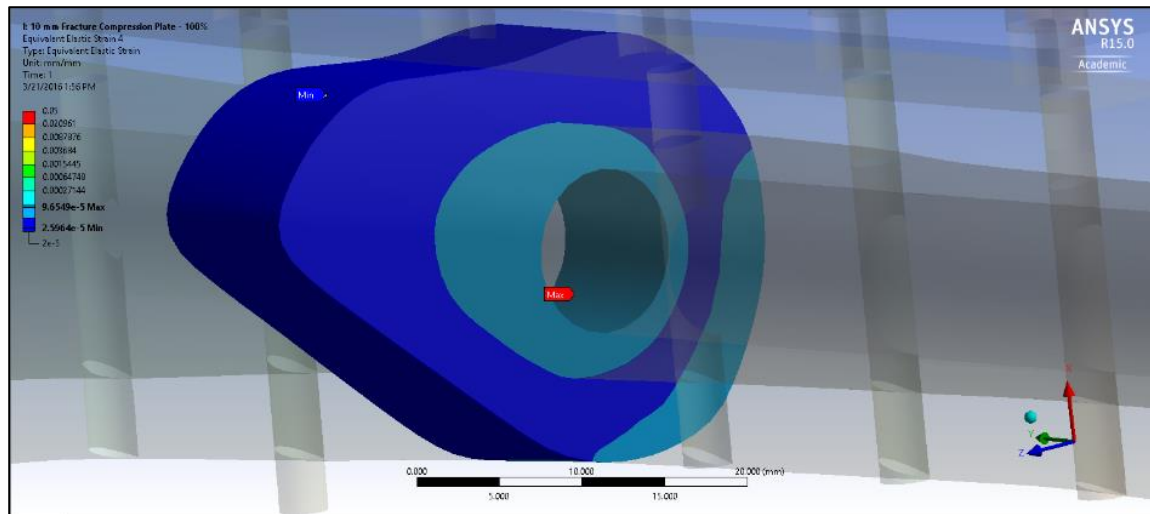


Figure 3. 15: 100% Callus stiffness model – Fracture Callus Equivalent Strain Distribution

The fracture callus models show regions of high equivalent strain in the cancellous bone tissue geometry under the 400 N (half body weight) compression loading condition. In addition, equivalent strain tends to be higher in regions located further away from the orthopedic plate. Strain within the fracture callus also decreased significantly in models with higher callus stiffness.

A summary of fracture callus equivalent strain results between 0.001% - 100% callus stiffness is shown in Figure 3. 16 below.

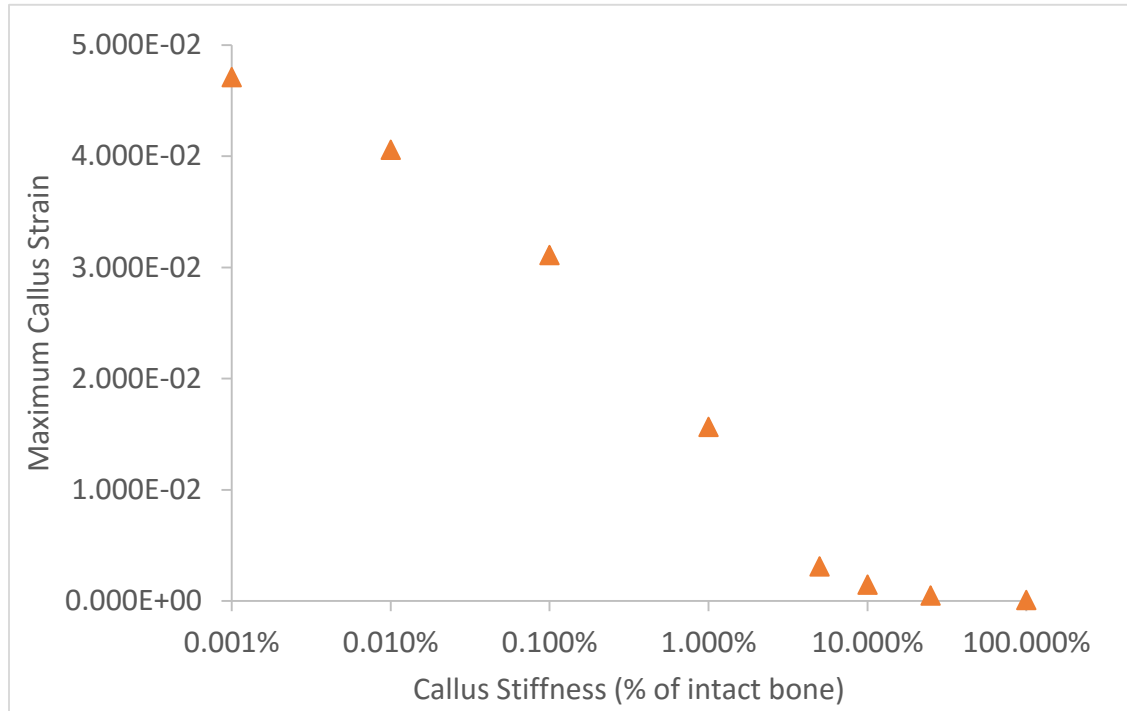


Figure 3. 16: Fracture Callus FEA Summary – Callus Strain v/s Callus Stiffness

Figure 3. 16 shows maximum callus equivalent strain on the vertical axis and callus stiffness on the horizontal axis on a logarithmic scale. According to the finite element models, equivalent strain within the fracture callus decreases rapidly as fracture stiffness increases from 0.001% - 100% of intact bone stiffness. These results show that fracture callus strain behaves similarly to orthopedic plate strain as the bone heals. The highest callus strain occurred in the 0.001% callus stiffness model at a value of 4.712×10^{-2} . Callus strain decreased until approximately 25% callus stiffness where it plateaued around 9.655×10^{-5} .

Discussion

The primary goal of the fracture callus finite element models was to simulate the process of bone healing from a mechanical perspective by varying the mechanical properties of the fracture callus. The equivalent strain distribution along the length of the orthopedic plate showed high equivalent strain above and around the fracture site in low callus stiffness models, which represent early stages of bone healing. Equivalent strain within the plate decreased rapidly with increases in callus stiffness until the strain distribution became relatively uniform in the 25% and 100% callus stiffness models. The higher stiffness models represent mid to late stages of bone healing where the majority of load sharing has shifted from the orthopedic plate to the healing bone. This trend agrees with prior studies using strain gauges with external fixation. Burny et al. mechanically tested 390 fractured long bones to look at bone flexion over time for normal healing, slow healing, delayed union and other complications [26]. They found that the fixation implants on bones undergoing normal healing saw the same rapid decreasing trend in flexion as the bone healed. Implant and callus response under other bone healing conditions could also be examined with variations to the finite element model.

The models agree with simpler representations of the internal fixation system as well. Models based on spring and beam theory were created to compare with finite element results. A diagram of the fixation system represented as a set of springs is shown below in Figure 3. 17.

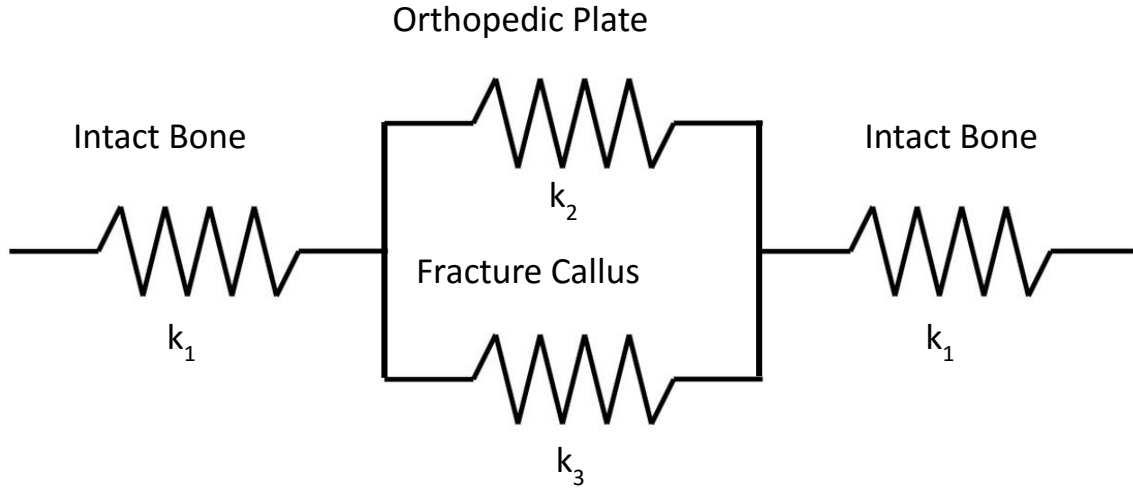


Figure 3. 17: Spring model of internal fixation system.

The governing equations of this simple spring model are Hooke's Law and the equivalent spring constant equations for series and parallel springs are shown below:

$$d = F/k$$

$$k'_{par} = \frac{k_2 * k_3}{(k_2 + k_3)}$$

$$k = k_1 + k_{par} + k_1$$

where d is displacement, F is force, and k represents the spring constant.

This model represents the fracture callus and orthopedic plate as a set of two springs in parallel that is connected to two additional springs in series that represent the intact bone. When intact bone stiffness is defined as $k_1 = 1$ and the relative stiffness of the fracture

callus is varied from 0 to 1, the relative displacement of the system can be calculated. The results of this model are shown in Figure 3. 18.

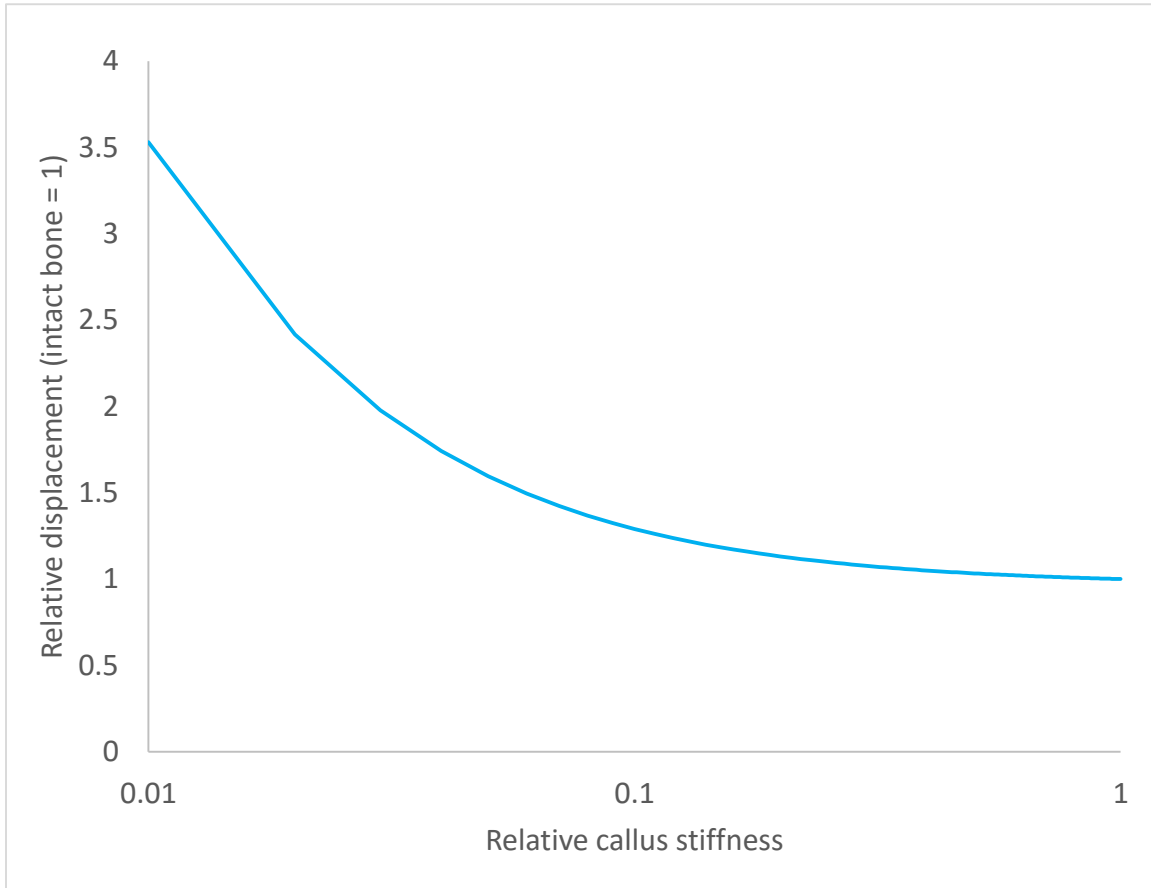


Figure 3. 18: Results of spring model – Relative Displacement v/s Relative Callus Stiffness.

Figure 3. 18 relates relative displacement of the system to relative callus stiffness (from 0 to 1). Relative callus stiffness is shown on the horizontal axis on a logarithmic scale. The simple 1-D spring model results in a similar hyperbolic relationship with a horizontal asymptote at a relative displacement value of one found in the strain and deformation results of the finite element models.

Beam theory offers a more complex 2-D model of the internal fixation system. Bourgois and Burny derive equations for fracture deformation and plate strain with cantilever beam equations from beam theory [14]. They considered a variety of loading cases including tension and bending. The cantilevered beam analyses revealed the same hyperbolic relationship between system elongation versus percentage of healing in the tension case and plate strain versus percentage of healing in the bending case.

Present and past work is limited to indirect methods for objective monitoring of interfragmentary strain and motion. These methods typically include tracking the mechanical response of implants or the use complex sensors and measurement systems that require specialized equipment and training. Direct measurement of fracture callus strain is usually impractical due to the limitations from surgery and bone healing interference. A finite element model capable of accurately approximating strain within the fracture callus would be a valuable tool in orthopedic implant design. Effective finite element approximations of the callus would also allow for optimization of the bone healing process through post-operative therapy tailored to maintain a range of callus strain that would improve healing time. The design of orthopedic implants themselves would also benefit as previous work has shown that a specific range of implant stiffness can accelerate bone healing[19,27].

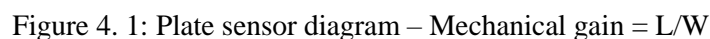
The maximum strain within the callus also followed the hyperbolic trend found in the orthopedic plate strain finite element results with increasing callus stiffness. While this is an expected result from previous studies [14,26], it is important to relate the approximated mechanics of the callus to that of the orthopedic plate and other implant

hardware to develop effective implant-mounted measurement devices that take full advantage of this relationship. Based on the results of the models and of prior studies, the early stages of bone healing are the most critical when monitoring the healing process.

The results of the callus stiffness models were used in conjunction with the orthopedic screw models in the development of a passive plate strain sensor capable of monitoring bone healing through changes in load sharing between an internal fixation implant and a human tibia. Understanding the relevant range of callus and plate stiffness was of particular importance in designing this device. Based on the finite element model results, the sensor should be capable of responding to a callus stiffness range of 0-10% of intact bone stiffness. The sensor should also be capable of responding to a maximum callus strain of ~ 0.05 to be effective at monitoring the healing progress of a fractured tibia.

Design Concept

The plate sensor design uses a simple cantilevered indicator pin that spans the length of the fracture site and moves relative to the opposite end of the plate. As the plate bends under load, the free end of the indicator pin remains stationary, resulting in a change in relative position that can be tracked with radiography and an internal scale. This design is a passive, purely mechanical solution that does not require any specialized equipment or power supply to use. The cantilevered indicator pin also provides mechanical gain roughly equivalent to the ratio between pin length from the fulcrum and the width of the bone. A diagram of the system that further explains the mechanical gain is shown in Figure 4. 1,



where L represents length of the pin past the fulcrum point, W represents width of the bone, a represents interfragmentary motion, and b represents relative motion between the free end of the pin and the rest of the system. The mechanical gain provided by the device can be calculated with geometric equations for the similar triangles shown in Figure 4. 2 and the equation below.

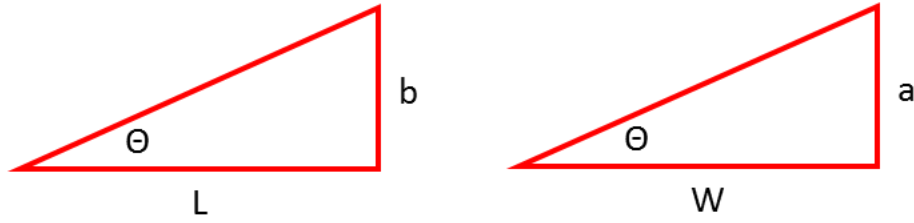


Figure 4. 2: Similar triangles that define the mechanical gain of the system.

$$Gain\ Factor = \frac{L}{W} = \frac{b}{a}$$

For example, a system with a bone thickness of 25 mm and a pin length of 125 mm would provide a mechanical gain factor of five. This mechanical gain is important because interfragmentary motion is typically small and difficult to monitor with standard radiography. This amplification of interfragmentary motion allows for a more robust measurement system.

Proof of Concept Model

Measuring the relative motion of the indicator pin to the orthopedic plate with radiography requires a radiopaque internal scale of known dimensions. A small scale was machined with two columns of 0.5 mm holes equally spaced 0.5 mm from one another to

serve in a proof of concept model. The proof of concept model included an internal fixation plate attached with a set of orthopedic screws to a fractured Sawbones tibia. The scale and indicator pin (0.5 mm diameter tungsten rod) were attached to an internal fixation plate with adhesive. The proof of concept model is shown in Figure 4. 3 below.

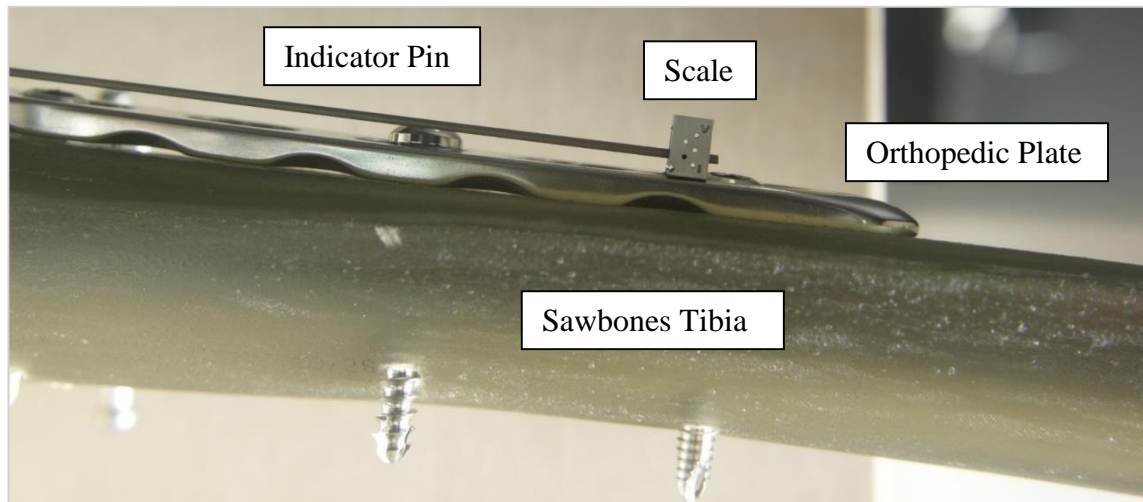


Figure 4. 3: Plate sensor – Sawbones proof of concept model

The Sawbones proof of concept model was loaded in compression with a Mark-10 motorized testing stand and the relative motion of the indicator pin was captured with both a camera and radiography. The sensor successfully responded to plate bending and the change in pin position could clearly be seen with x-ray imaging, as shown in Figure 4. 4. The pin moves from covering the first scale hole to covering the second as the applied load and subsequent plate strain increases.

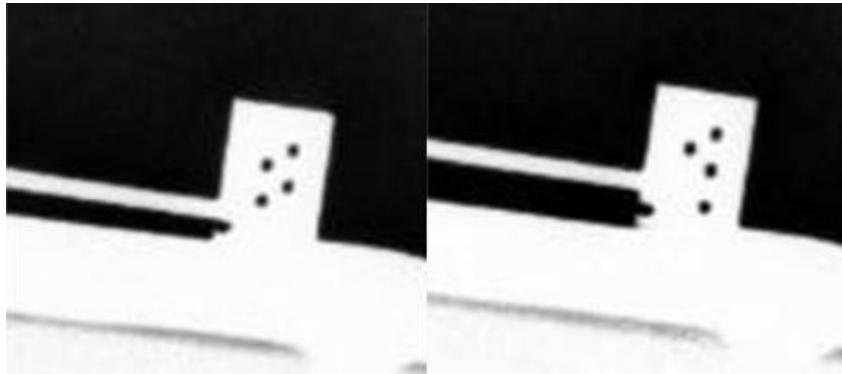
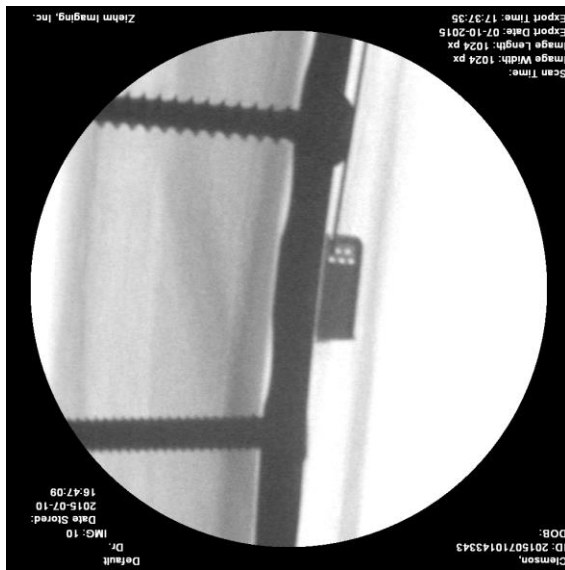


Figure 4. 4: X-ray images of internal scale and indicator pin.

The proof of concept model was also tested in a human cadaver trial. One of the primary goals of this trial was to assess the installation requirements of an internal fixation mounted sensor in a surgical setting. Another goal of this trial was to repeat the Sawbones mechanical test to assess sensor response under compressive loading of a human tibia while also developing a cadaveric testing protocol for future cadaver trials of more refined sensor prototypes. Details of the experimental methods of the cadaver trials can be found in the “Methods” section of this chapter. Radiography images of the cadaver testing with the proof of concept model are shown in Figure 4. 5 for the intact tibia case and Figure 4. 6 for the fractured tibia case.

0 N Force



400 N Force ($\frac{1}{2}$ body wt)

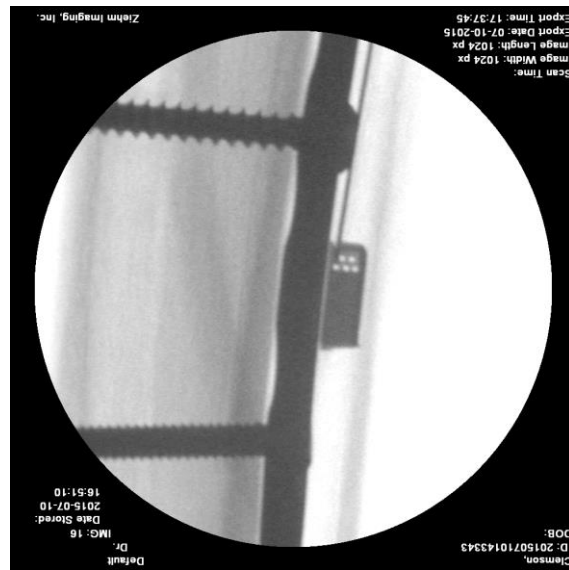


Figure 4. 5: First Cadaveric Trial – Sensor response with intact tibia.

0 N Force



300 N Force

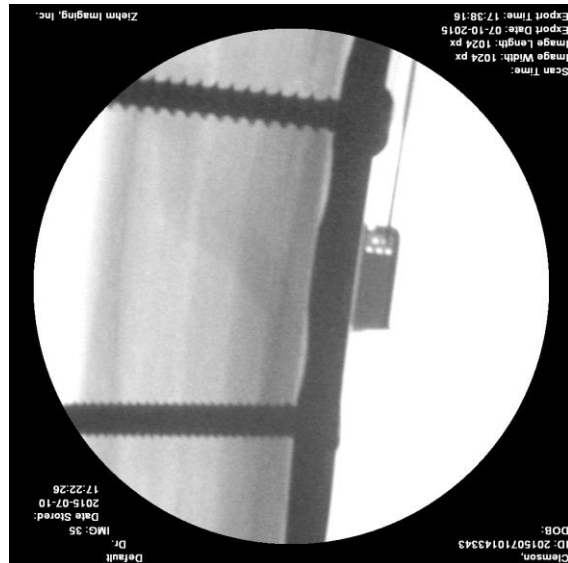
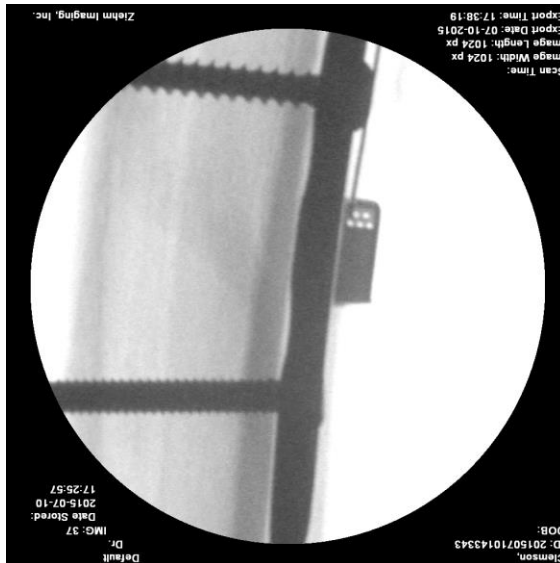


Figure 4. 6: First Cadaveric Trial – Sensor response with fractured tibia.

Sensor Prototype

The passive sensor device consists of two components fabricated from stainless steel and a 0.5 mm diameter tungsten indicator pin. Tungsten was chosen as the indicator pin material since it is highly radiopaque. The two stainless steel components are machined to match the profile of an existing orthopedic plate. One of the stainless steel components is positioned on the side of the fracture near the proximal end of the tibia and supports the cantilevered tungsten pin on the side of the orthopedic plate. The second stainless steel component is secured on the end of the orthopedic plate nearest the distal end of the tibia on the opposite side of the fracture and features an internal scale. These components can be secured to the plate via clamping forces applied by a single set screw located on the side of each component. A Synthes 4.5 mm proximal tibia plate was used in the sizing and testing of this device. The sensor system is shown in Figure 4. 7.

The internal scale consists of five 0.5 mm diameter holes that are precision machined into the second component. The holes are positioned in two columns and have an equal spacing between them of 0.5 mm in both the vertical and horizontal directions. The tungsten indicator pin is manually bent to match the contour of the plate and to align the pin tip to a starting position relative to the scale. The scale provides an objective measure of relative displacement between the indicator pin and the orthopedic plate. Plate bending, interfragmentary displacement, and fracture strain can then be derived from the relative displacement of the pin. Five potential readings are possible from the indicator pin covering one of the scale holes completely. Another five potential readings result in the indicator pin resting between two holes, resulting in partial coverage of both. The last

potential reading is the indicator pin resting below the first hole in the starting position. The simplicity of the internal scale allows clinicians to obtain measurements without specialized training or radiographic techniques.

A rigid pin cover was fabricated using 3-D printing and transparent PLA filament. However, the pin cover must be sufficiently flexible to conform to the contour of the orthopedic plate once it is bent along the tibia. Manual customization of the pin cover contour during surgery is beneficial due to variations in bone geometry, fracture locations, and orthopedic plates. Additional pin covers were fabricated with the flexible filament NinjaFlex® provided by NinjaTek™. These covers were capable of bending with the plate after installation without interfering with the indicator pin, however the increased flexibility prevented secure attachment to the orthopedic plate. Printing the pin cover with rigid filament at anchor points and flexible filament elsewhere should provide secure attachment to the plate at appropriate intervals while maintaining flexibility along the length of the pin cover.

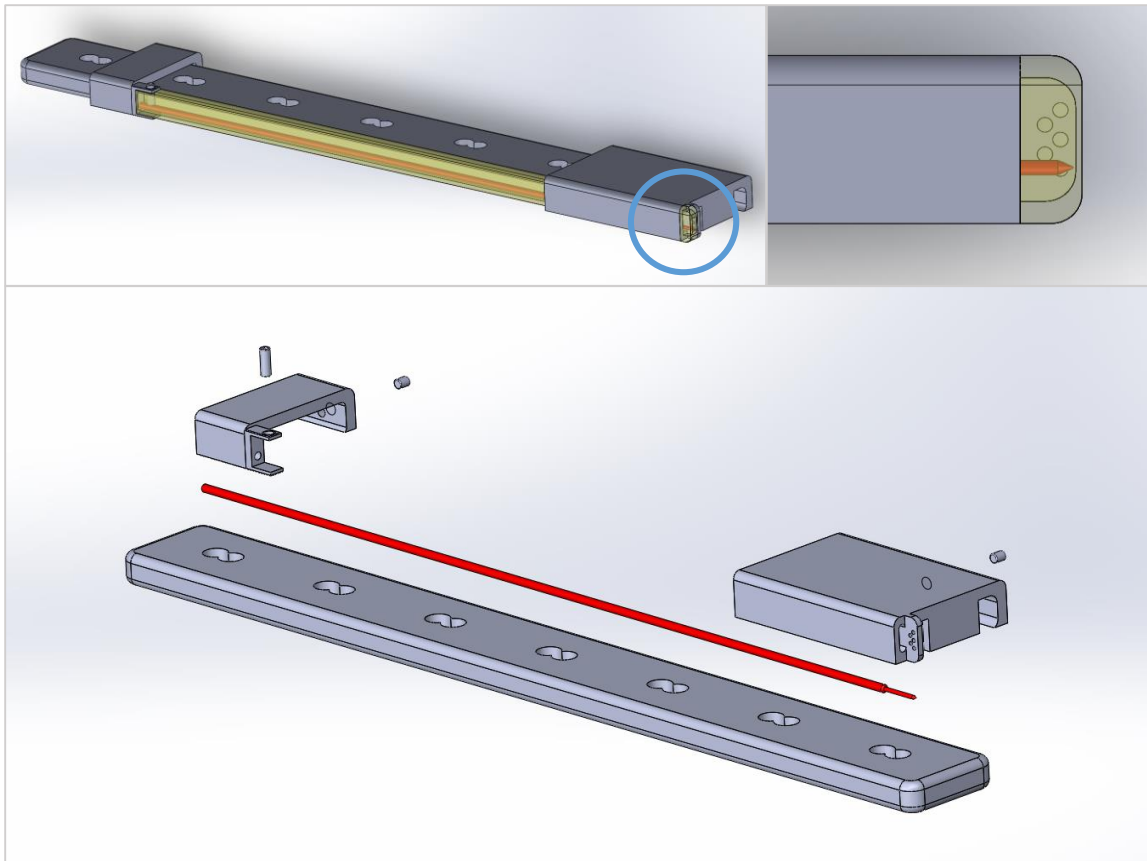


Figure 4. 7: Passive strain sensor design. (A) Assembly of passive strain sensor components mounted to an orthopedic plate. (B) Internal scale component. (C) Exploded view.

Methods

Plate Sensor Prototype FEA

A solid geometry of the prototype sensor was added to the callus stiffness models presented in chapter 3 to compare the approximated sensor response to plate strain, interfragmentary strain, and callus stiffness under the 400 N compression loading condition. The callus stiffness was varied between 0.001% - 100% of intact bone stiffness.

Cadaveric Trials - Experimental Setup

The sensor prototype was tested in a cadaveric biomechanical proximal tibia fracture model to evaluate the effectiveness of the passive sensor in indicating implant bending with standard radiography. In each test, a Synthes 4.5 mm proximal tibia plate was surgically implanted on a human cadaver tibia with a set of orthopedic screws. The indicator pin support and internal scale components were then attached to the orthopedic plate on either side of the fracture and secured with set screws. A 0.5 mm diameter tungsten indicator pin was then installed and secured with adhesive before being bent to align with the contour of the plate and internal scale.

The specimen was secured to a Mark-10 motorized testing stand in an anatomical stance for compression testing, as shown in Figure 4. 8. The goal of the test was to monitor the sensor response using radiography under a series of compressive loads with both intact and fractured bone. The intact human cadaver tibia was loaded in compression from 0 – 400 N in 100 N increments and the sensor response was recorded with radiography. Both the sensor response and the resolution of the internal scale with standard radiography were

examined. An unstable fracture was then introduced to the human cadaver tibia. The fractured specimen was subjected to a series of compressive loading cycles, first from 0 – 200 N in 25 N increments and second from 0 – 100 N in 25 N increments. The sensor response was again recorded with radiography at each loading step. X-ray images of the fracture site were also recorded at 0 N and 400 N loads for resolution comparisons with the internal scale measurements of interfragmentary motion.

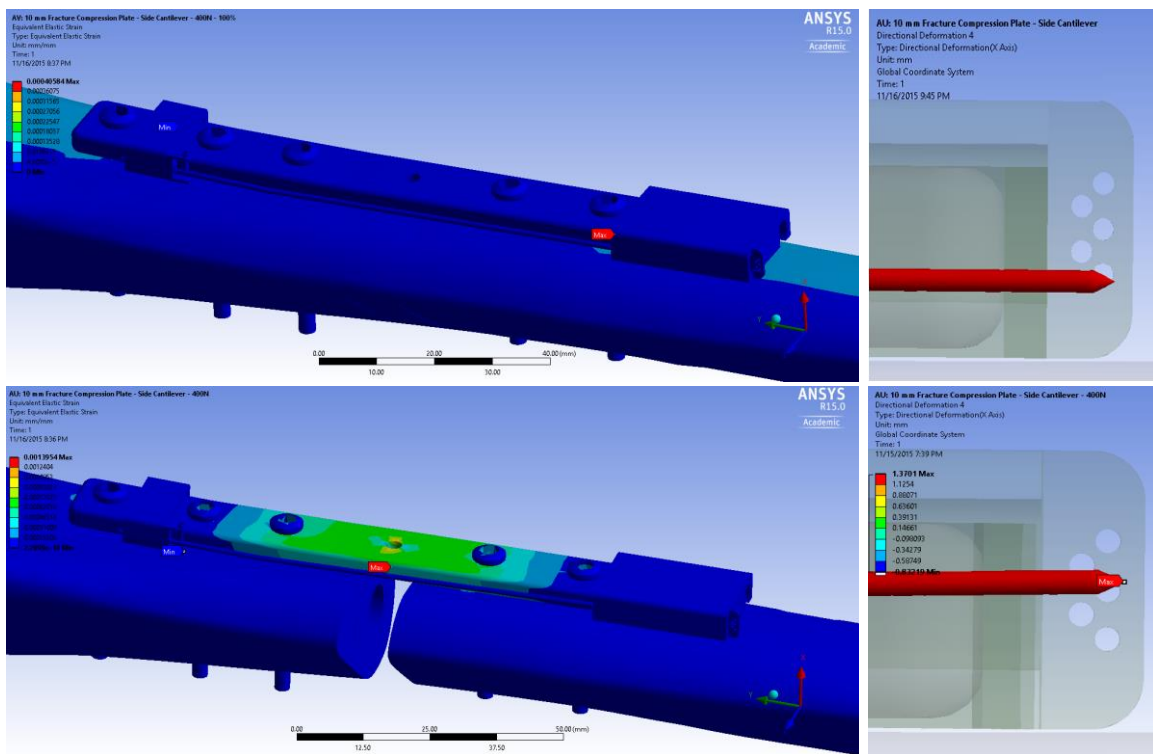


Figure 4. 8: Cadaveric mechanical test setup with Mark-10 motorized testing stand.

Results

Plate Sensor Prototype – FEA Results

The intact tibia model (100% callus stiffness) under the 400 N compressive loading condition resulted in very little displacement of the indicator pin relative to the internal scale. However, the 10 mm fracture model showed 1.45 mm (sensor reading between holes 3 and 4) of indicator pin displacement relative to the internal scale under the same loading condition. The strain distribution of the system and the corresponding sensor response in each of these cases are shown in Figure 4. 9.



The prototype strain sensor geometry was also applied to the finite element models of varying callus stiffness to assess sensor response as the bone heals. These models used the 400 N loading condition as well. A plot comparing sensor response and maximum callus strain against increasing callus stiffness is shown in Figure 4. 10.

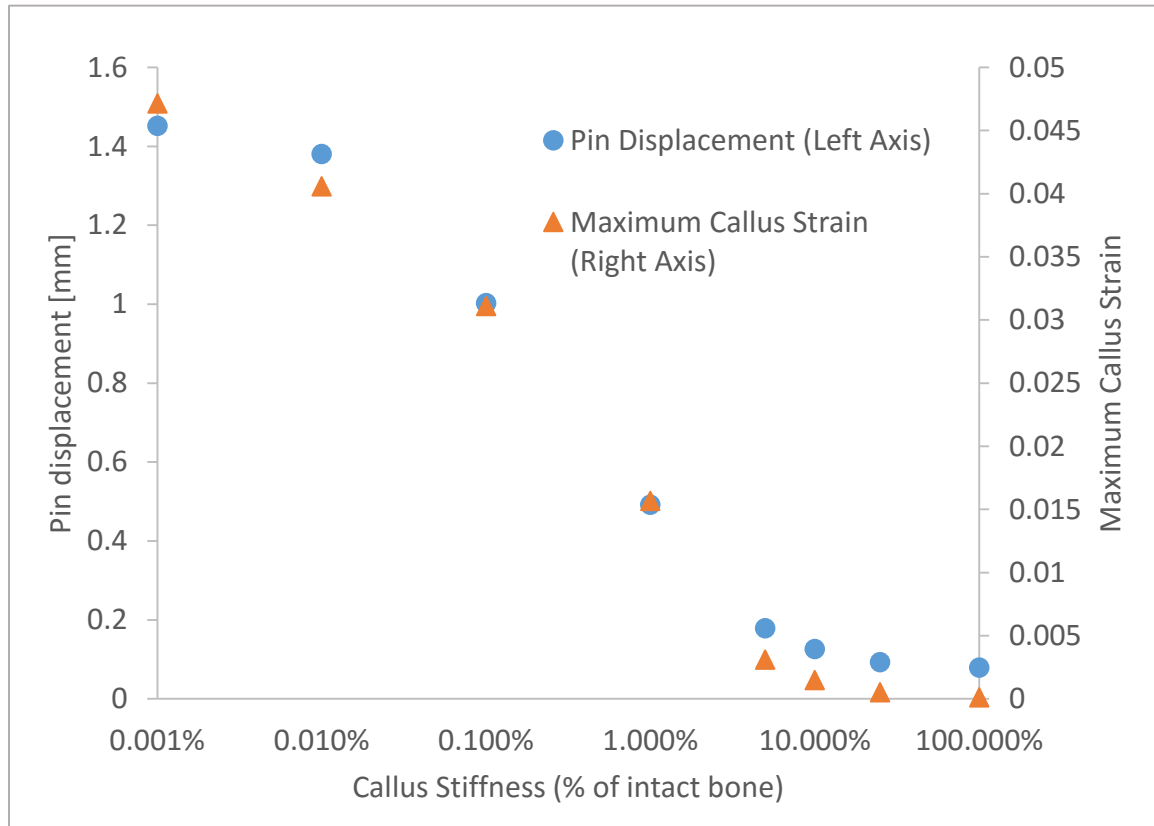


Figure 4. 10: Pin displacement and maximum callus strain v/s callus stiffness.

The graph in Figure 4. 10 shows pin displacement relative to the orthopedic plate in millimeters and maximum callus strain resulting from increases in callus stiffness as shown on a logarithmic scale on the horizontal axis. The relationship between callus stiffness and pin displacement is shown in Figure 4. 11.

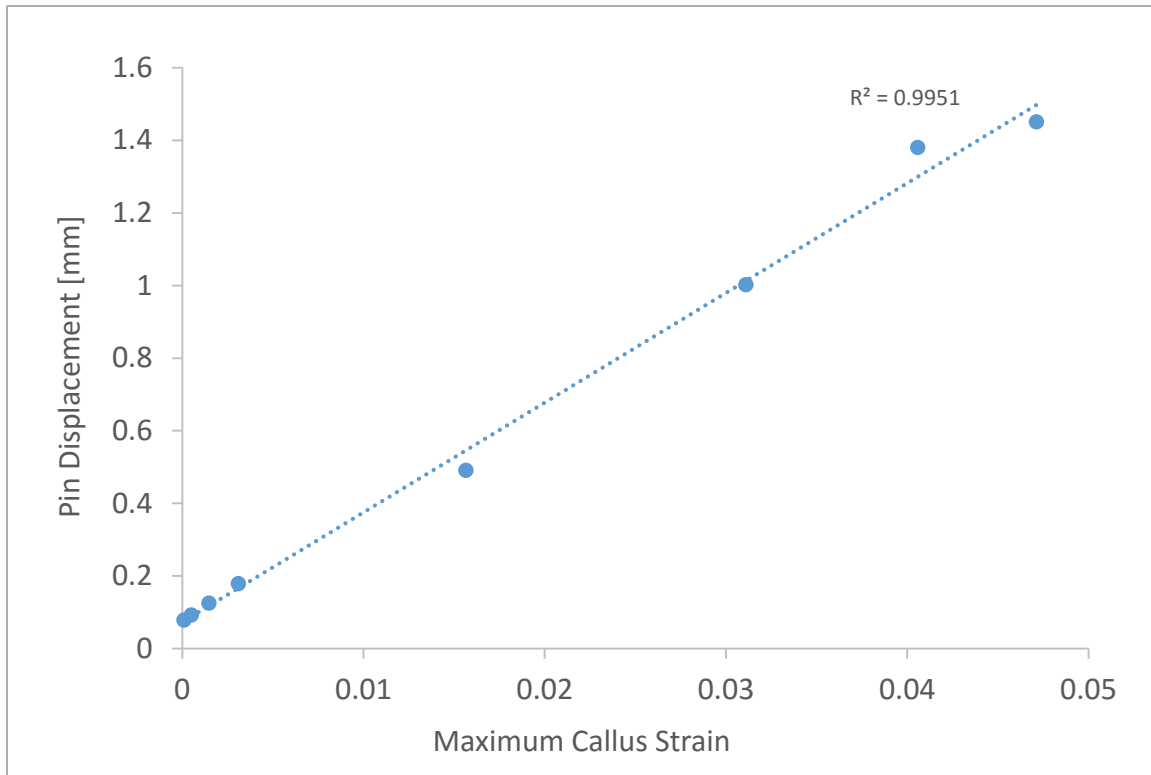


Figure 4. 11: Linear relationship between relative pin displacement and maximum callus strain.

The relationship between the prototype sensor response and fracture callus strain was mostly linear based on a summary of the results from the callus stiffness models. These results indicate that the prototype sensor responds to 1.5% callus strain with ~0.5 mm of relative pin displacement.

Plate Sensor Prototype – Cadaver Trial Results

The passive strain sensor prototype designed to monitor plate bending appropriately responded to compressive loading during human cadaver tibia testing. Submitting the intact tibia to compressive loading resulted in no discernable change in the position of the indicator pin with radiography. However, once an unstable fracture was introduced to the tibia, steady movement of the indicator pin relative to the internal scale through radiography as the compressive loading increased was clearly identifiable. The indicator pin moved from covering the first hole on the internal scale to the final hole around 200 N. A plot of relative pin displacement with compressive loading from 0-100 N is shown in Figure 4. 12.

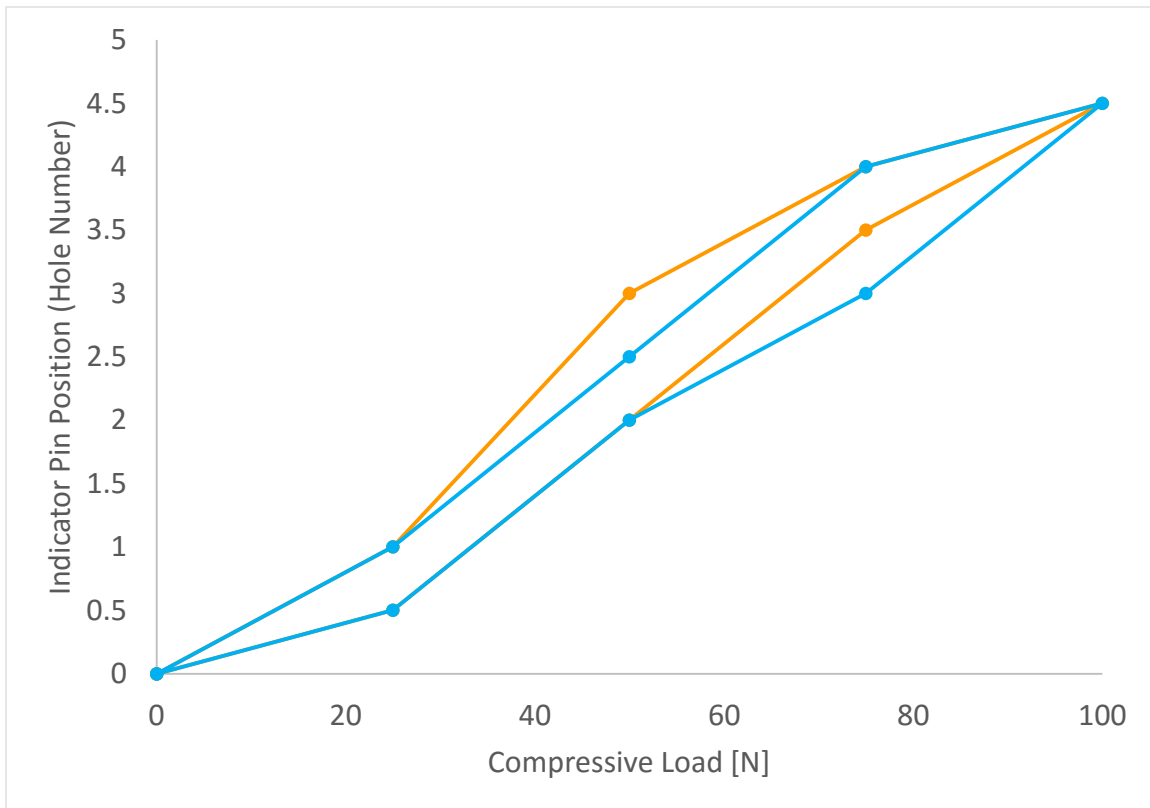


Figure 4. 12: Second Cadaveric Trial – Sensor Response v/s Compressive Load

The indicator pin also successfully returned to the starting position when the compressive load was removed in each of the loading cycles. Measurements from the sensor were easily read compared to tracking interfragmentary motion and plate bending with radiography images of the fracture gap. Radiography images of the sensor response and the fracture gap are shown in Figure 4. 13. The indicator pin moved from below hole 1 when the tibia was unloaded and to hole 4 under the 100 N compressive load.

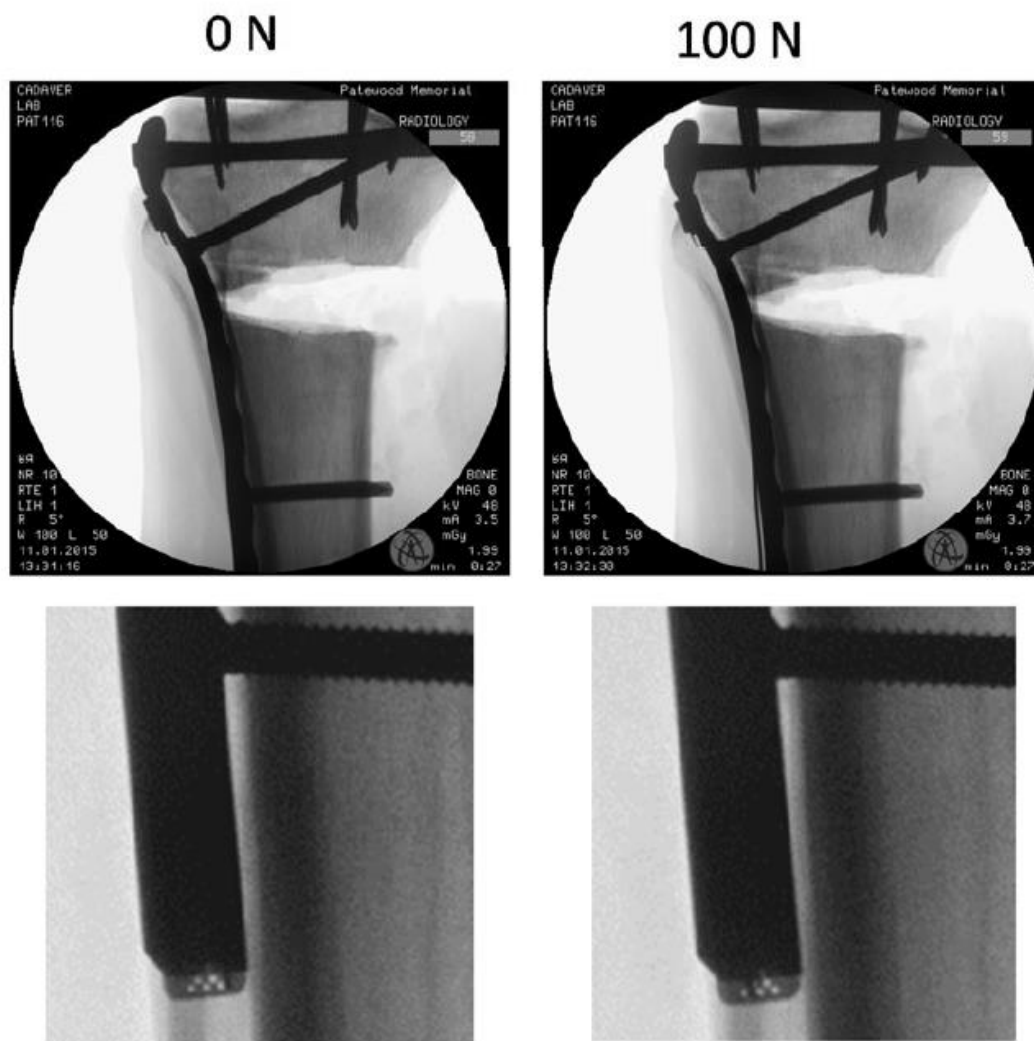


Figure 4. 13: Radiography images of the fixation implant, fracture gap, and strain sensor for both unloaded and 100 N compression loaded cases.

Discussion

The prototype strain sensor appropriately responded to plate bending by an increase in pin displacement relative to the internal scale in both the cadaver experiment and the finite element model. The sensor did not respond to the intact tibia under load because the bone was supporting the load instead of the plate. Once the 10 mm fracture was introduced, the plate supported the entire load across the fracture, resulting in pin displacement relative to the internal scale.

The FEA model shows that as the callus stiffens, the orthopedic plate shares less of the load and in displacement decreases. Eventually the callus stiffness is high enough to dominate the orthopedic plate, resulting in drastically reduced plate bending and sensor response. The linear increase in pin displacement with maximum callus strain in the finite element results implies that the sensor can effectively monitor callus strain indirectly through plate bending. The amount of pin displacement for a given callus strain was also significant. The results shown in Figure 4. 10 indicate that ~1.5% callus strain causes ~0.5 mm of relative pin displacement. The prototype strain sensor can easily indicate 0.5 mm of relative pin displacement since each hole on the scale is 0.5 mm in diameter. The callus strain increment of 1.5% was also significant because up to 2% interfragmentary strain has been shown to be conducive to primary bone healing [28].

We determined that the prototype strain sensor can be read clearly through radiography images during human cadaver testing. The images containing the sensor provide objective readings of plate bending and interfragmentary displacement with a resolution of 250 μm , compared to 2-5 mm resolution of traditional x-ray assessment of

the fracture site. Figure 4. 13 showcases the difficulty of discerning interfragmentary motion with radiography of the fracture site alone compared to using the internal scale and indicator pin. The sensor successfully tracked plate bending and interfragmentary displacement with both increasing and decreasing axial loading of the tibia with adequate repeatability. The position of the indicator pin nearly reached its limit at 100 N of axial loading during human cadaver testing. This response is to be expected as the orthopedic plate is supporting all of the load due to the absence of a fracture callus early in healing. As such, a patient would not be able to bear weight at this stage. Eventually, the callus becomes stiff enough to support enough load from the orthopedic plate to allow for safe weight bearing without risk of implant fatigue failure.

The sensor did not require specialized orientations or imaging techniques to be read. Only traditional x-ray imaging was required. The internal scale was also insensitive to reasonable changes in viewing angle and sample position, resulting in robust measurements and standardized results between multiple patients and instruments. This quality also improves comparisons of bone healing with respect to time. The working principle of this sensor can be translated to other potential applications including spine fusion and hip fracture fixation.

The mechanical gain of the sensor prototype design is based on the long indicator pin. The mechanical gain of the system can be further improved with increases to pin length or the incorporation of gears, pivots, levers, or other gain mechanisms found in other applications. One example of other mechanical gain mechanisms is a common machinist's dial indicator. Although the mechanical gain was beneficial in increasing sensor response

to interfragmentary motion, the large length of the pin made it more susceptible to interference from coming into contact with the pin cover or surrounding tissue. The high flexibility of the pin that is necessary for manual calibration with the internal scale also contributed to this susceptibility. Design alternatives that decrease pin length or do not require low pin stiffness for calibration would make the sensor more robust.

CHAPTER FIVE

CONCLUSIONS AND FUTURE WORK

The primary outcomes of the research work presented in this thesis can be divided into two categories. The first outcome was the development of a series of finite element models capable of approximating the mechanical environment of a human tibia treated with internal fixation. In total, 94 models were created to consider variants of implant geometry, fracture size, callus material properties and loading conditions. These models provided an initial step towards obtaining a valuable design tool capable of saving time and resources when developing orthopedic implants or devices that can monitor the mechanical behavior of a healing tibia.

The finite element analysis of the individual orthopedic screw resulted in an average screw elongation of 47 μm and a peak elongation of 55 μm , which was similar to an experimental elongation of 57-59 μm under a 1500 N load. This model not only reinforces the experimental results, but it can also be used to initially assess future design iterations of the screw-mounted strain sensors. The internal fixation system models also provided approximations for the appropriate range of orthopedic screw strain under a variety of clinically relevant loading conditions. Internal fixation system models that included fracture callus geometry and variable callus stiffness simulated the mechanical response of implants with respect to bone healing progress. These models approximated the strain distributions of the orthopedic plate and fracture callus at all stages of bone healing. These results revealed that the orthopedic plate relinquished the majority of load sharing to the healing bone at callus stiffness values greater than 10% of intact bone.

Therefore, monitoring load sharing at values of 0-10% callus stiffness is critical in the prevention of re-fracture from early weight bearing. The callus stiffness models also showed a common rapid decrease of strain with increasing callus stiffness in the orthopedic plate and the callus itself, confirming that changes in plate bending is an effective indicator of changes in callus stiffness. The hyperbolic pattern of plate and callus strain as bone healing progresses agrees with experimental results on external fixators as well [26]. Unlike with external fixation, there is currently no method of mapping the mechanical response of internal fixation implants for the wide range of bone healing outcomes. However, the finite element models developed for this work can be used in future studies that examine other potential outcomes of bone healing with internal fixation and compare with previous research results for external fixation mechanics with bone healing.

The second outcome of this work was the development of a passive, implant-mounted strain sensor prototype capable of monitoring bone healing through orthopedic plate bending at much higher resolutions than those available with current clinical methods. The sensor adds a mechanical gain factor roughly equivalent to the ratio of pin length to bone diameter. The proposed sensor provides physicians with an objective method to monitor fracture healing. The sensor consistently tracked interfragmentary displacement in human cadaver trials through standard radiography with $\sim 250\text{ }\mu\text{m}$ resolution, compared to 2-5 mm resolution with traditional radiography at the fracture site. Displacement measurements taken with standard radiography has also been found to have an inter-observer variation of 1-3 mm [15]. Higher resolutions with standard radiography are possible with in-depth image analysis, but this is limited by a high sensitivity to variations

in positioning and orientation of the patient during imaging. One of the primary strengths of the prototype strain sensor was its insensitivity to variations in image orientation while maintaining its high resolution. Initial FEA results showed the sensor was capable of measuring clinically relevant values of fracture callus strain as the bone heals. Therefore, the proposed sensor provides an effective, non-invasive method of objectively determining when a patient is safe for weight bearing. Furthermore, the sensor can be read clearly with standard radiography techniques without the need for specialized equipment, training or scanning orientations.

Additional work to improve and validate the finite element models is required. The current geometry and material properties of the models were based on those provided by Pacific Research Labs to maintain consistency with physical models commonly used experimentally. Currently, the model geometry for the cortical and cancellous bone tissue of the tibia is solid with adjusted material properties to account for the porosity of bone tissue in reality. Accuracy of the models may be improved with more advanced bone geometries that include more realistic bone structure. However, simulating bone tissue inherently includes large sources of variance from patient to patient and between bone types. More intricate geometries of bone tissue would also dramatically increase computation time and mesh complexity in three-dimensional models like those described in this document. These challenges mean that the models are more suited towards comparative analysis between implant and sensor designs, or in identifying general trends in mechanical response, rather than direct strain approximations of a particular case.

The prototype plate strain sensor design can be improved as well. The current design was susceptible to interference of indicator pin motion from contact with the pin cover or surrounding tissue. Calibrating the indicator pin by manually bending it to match the contour of the orthopedic plate was also awkward and detrimental to repeatability. The design can be improved by implementing other gain mechanisms that would allow for a shorter and stiffer indicator pin that would be less affected by interference from the surrounding environment. The sizing of the internal scale allowed it to be easily read with standard radiography. Future scale designs could continue using a series of 0.5 mm holes or tick marks of similar thickness to maintain clarity with images from radiography. Potential improvements to the prototype design could incorporate gears, levers, pulleys or other gain mechanisms to replace the long cantilevered indicator pin.

APPENDICES

Appendix A

Orthopedic Screw Strain – Other Loading Conditions

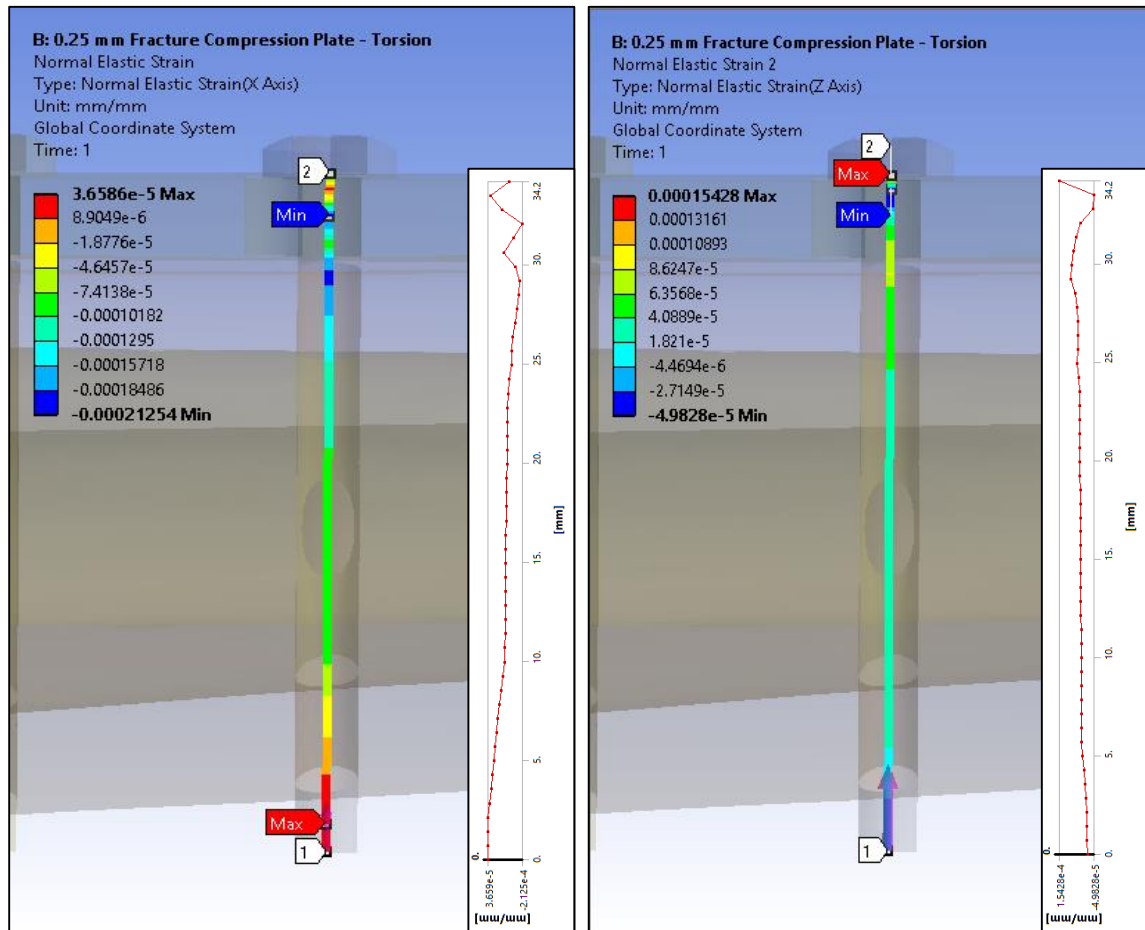


Figure A-1: 0.25 mm fracture – Screw strain distribution for 100 N·mm torsion.

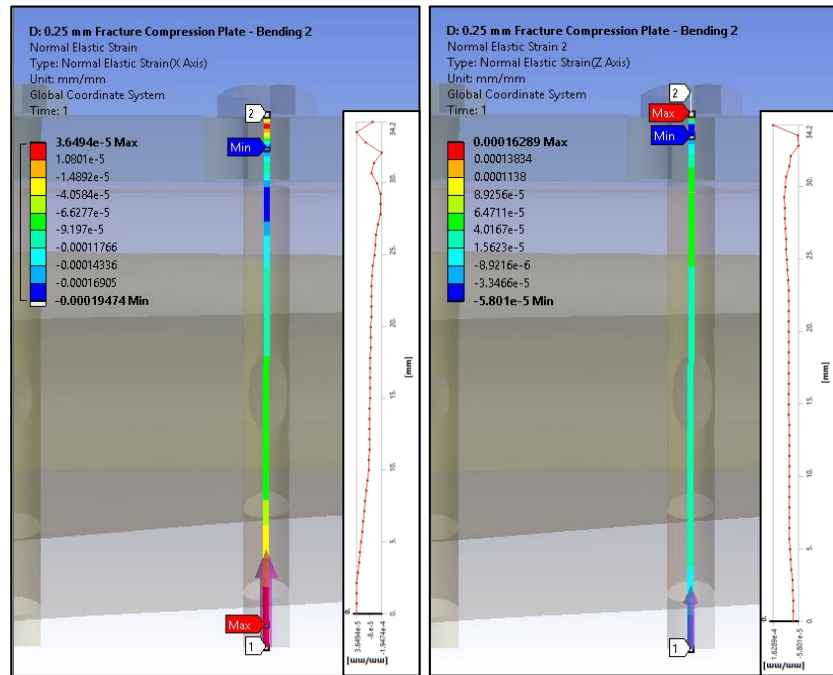


Figure A-2: 0.25 mm fracture – Screw strain distribution for 5,000 N sagittal bending.

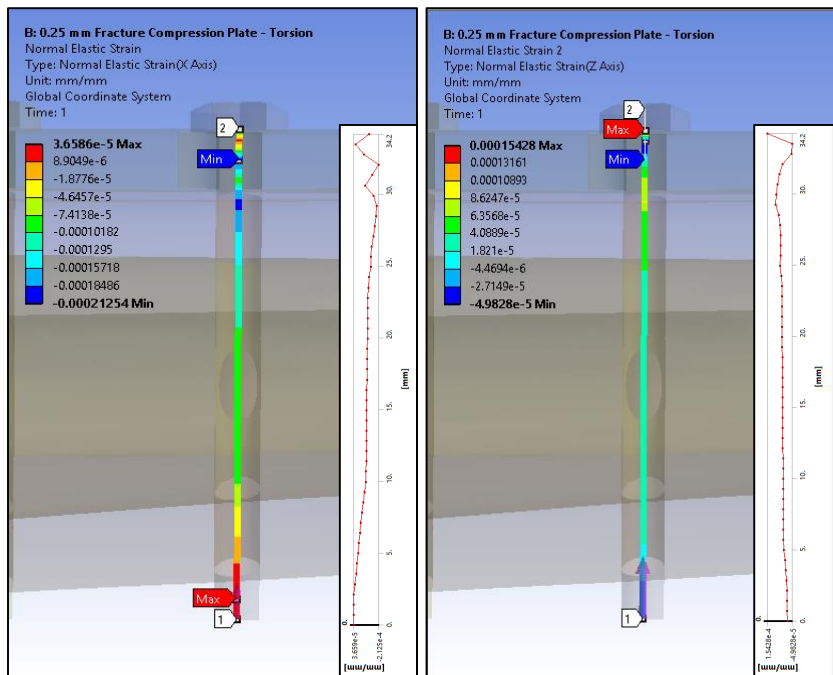


Figure A-3: 0.25 mm fracture – Screw strain distribution for 5,000 N coronal bending.

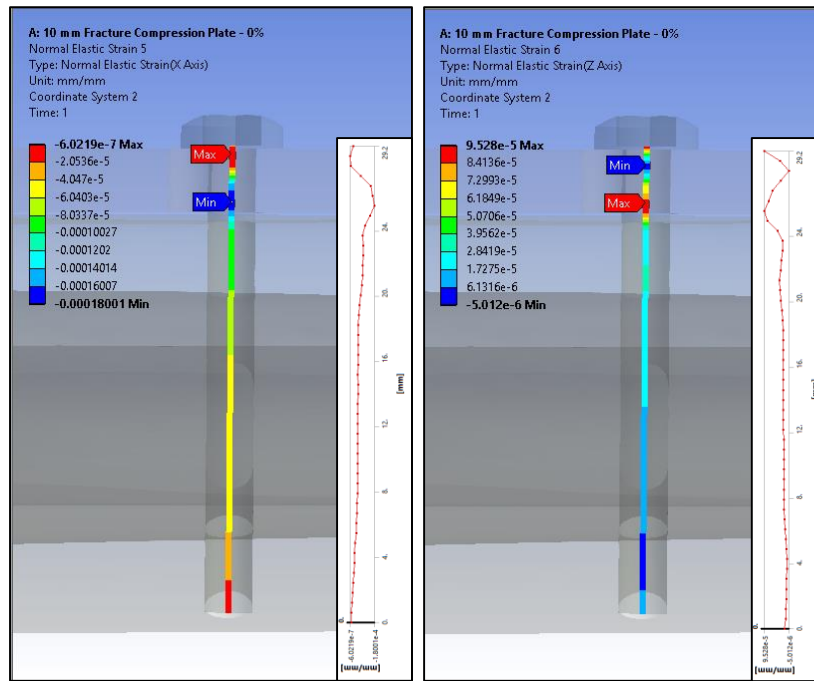


Figure A-4: 10 mm fracture – Screw strain distribution for 400 N compression.

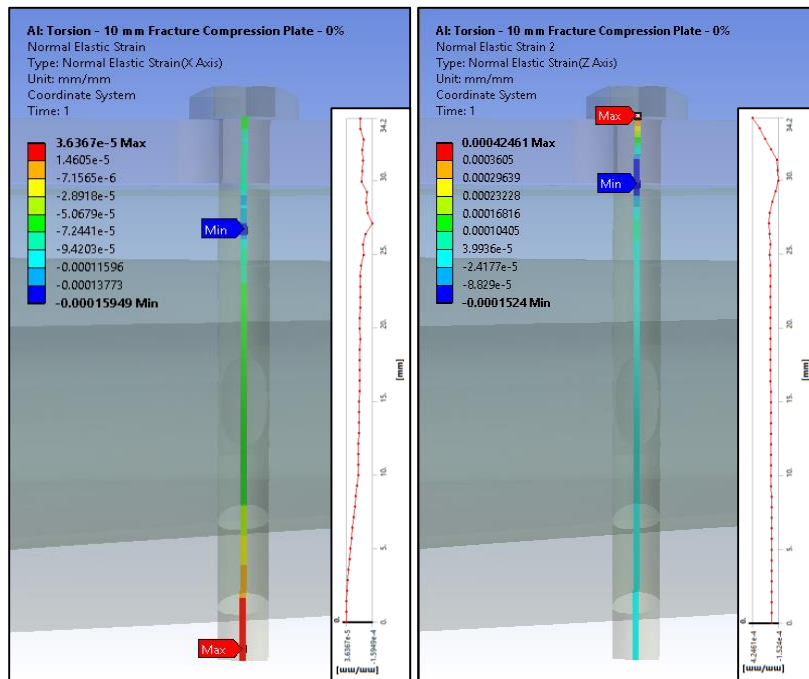


Figure A-5: 10 mm fracture – Screw strain distribution for 100 N·mm torsion.

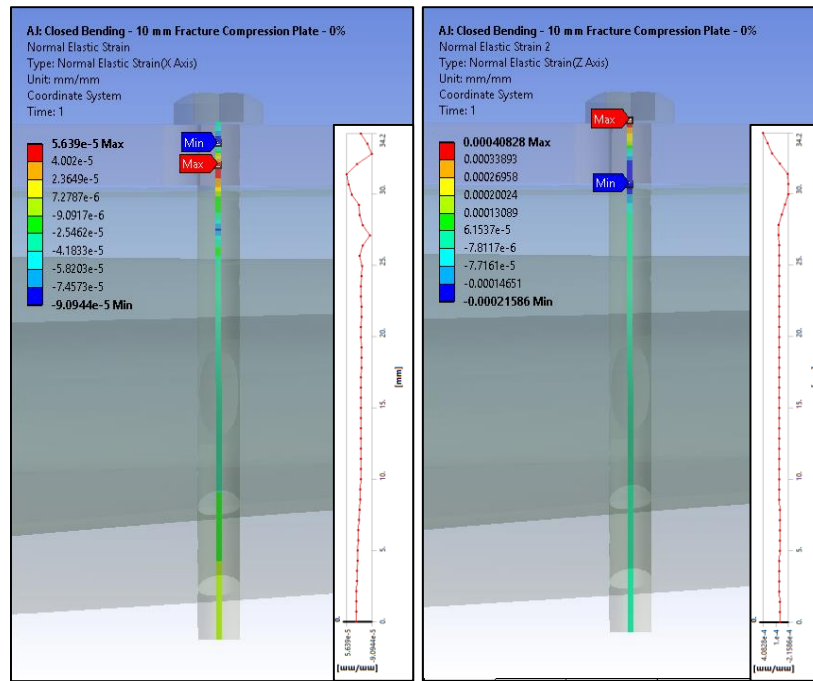


Figure A-6: 10 mm fracture – Screw strain distribution for 7,500 N·mm coronal (-X) bending.

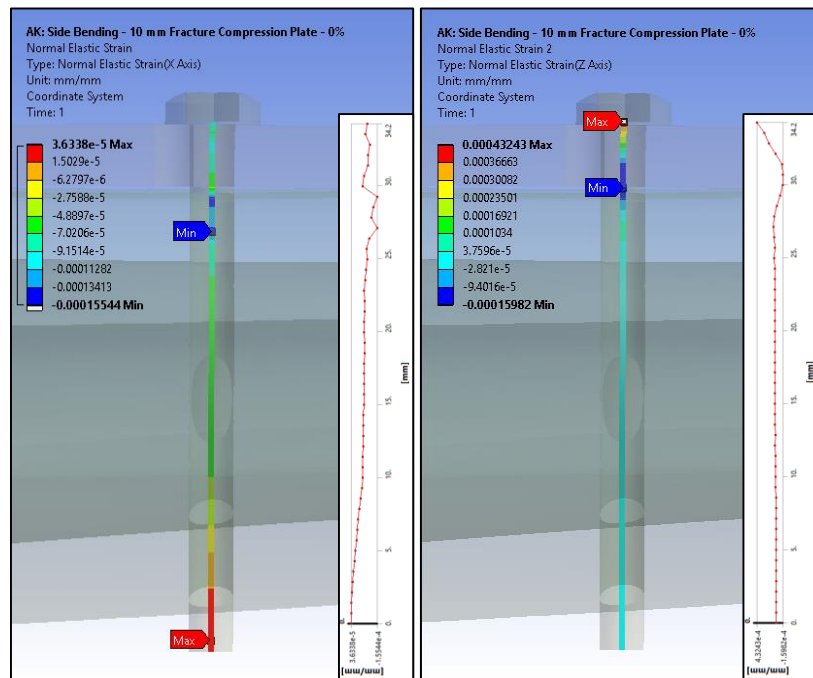


Figure A-7: 10 mm fracture – Screw strain distribution for 5,000 N·mm sagittal bending.

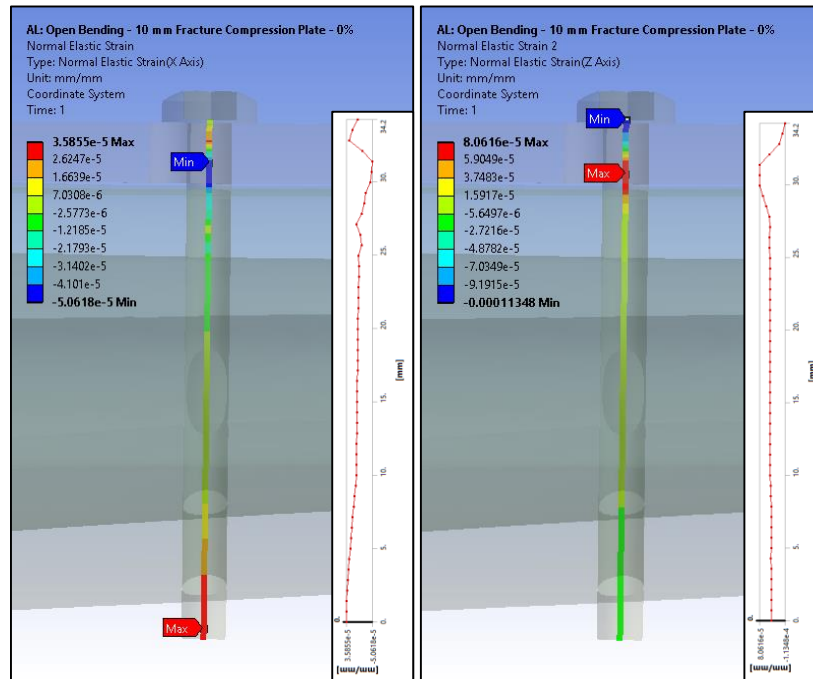


Figure A-8: 10 mm fracture – Screw strain distribution for 7,500 N·mm coronal bending.

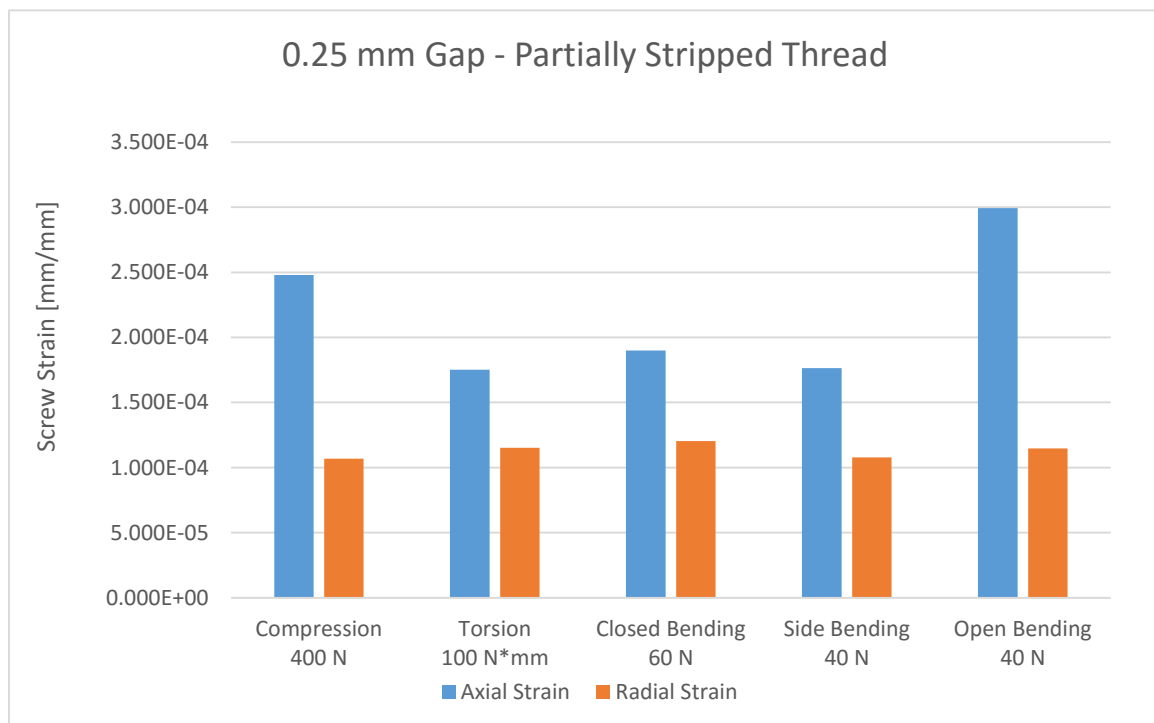


Figure A-9: 0.25 mm fracture – Partially stripped thread – Maximum screw strain.

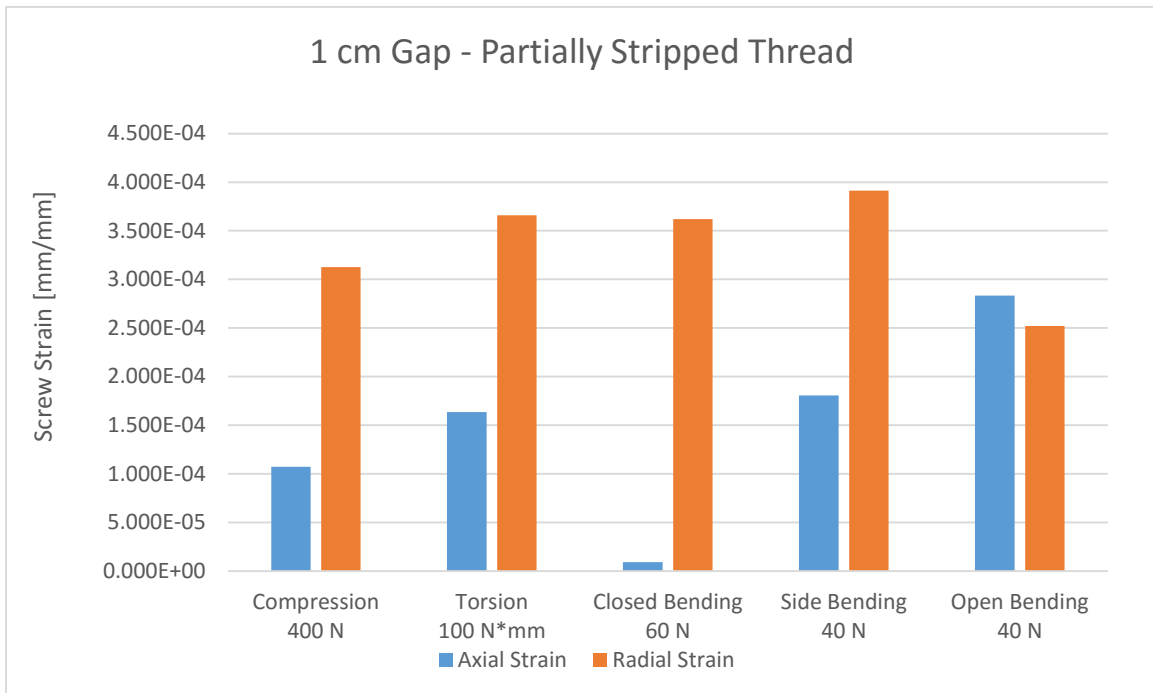


Figure A-10: 10 mm fracture – Partially stripped thread – Maximum screw strain.

Orthopedic Plate Strain – Other Callus Stiffness Models

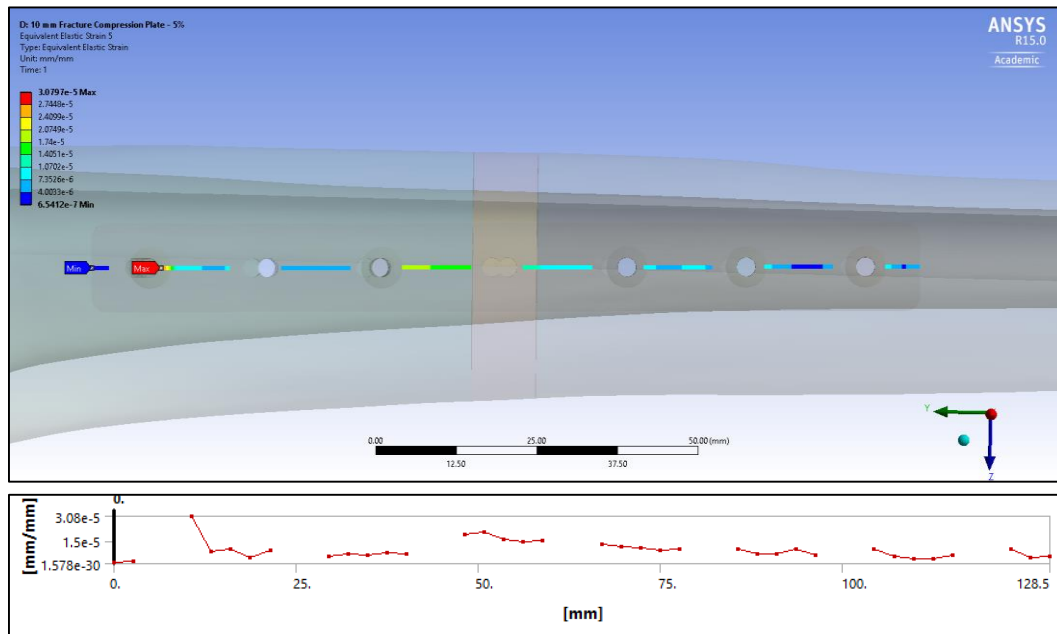


Figure B-1: 5% Callus stiffness – 400 N Compression – Plate center strain distribution.

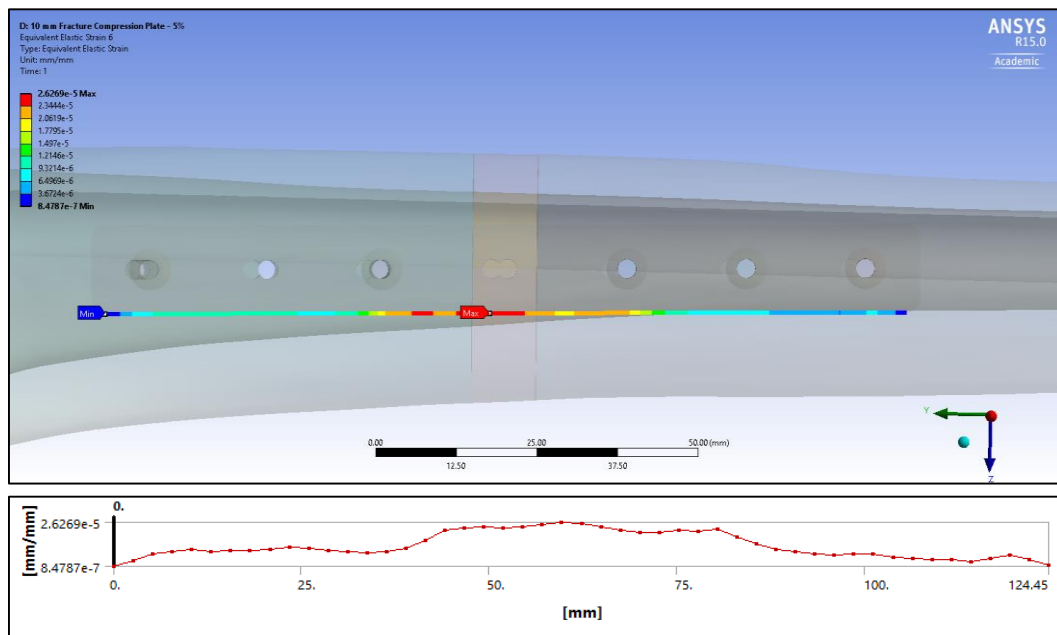


Figure B-2: 5% Callus stiffness – 400 N Compression – Plate side strain distribution.

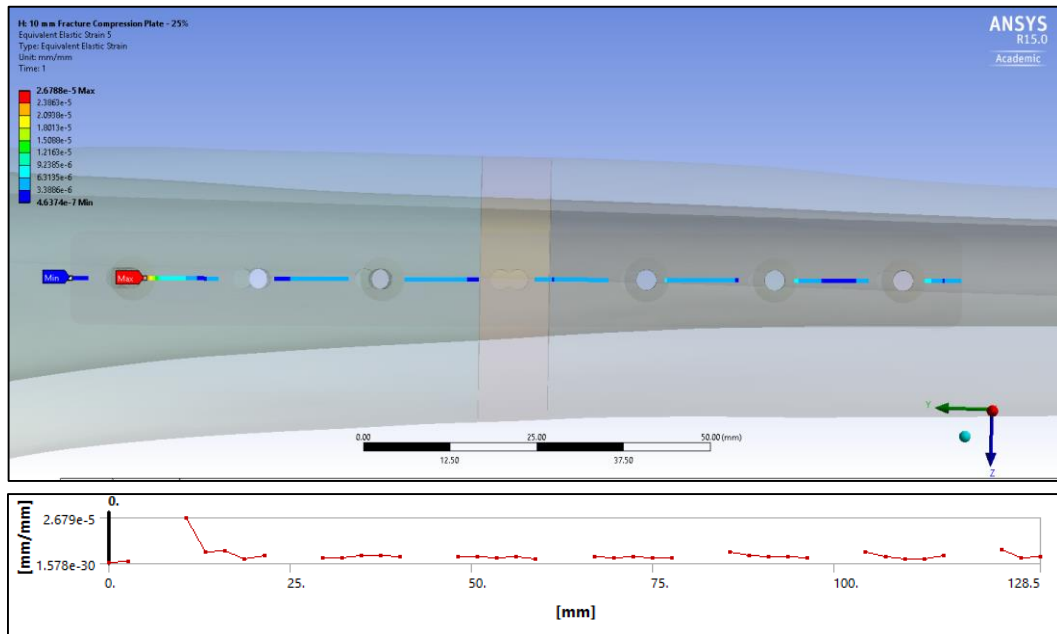


Figure B-3: 25% Callus stiffness – 400 N Compression – Plate center strain distribution.

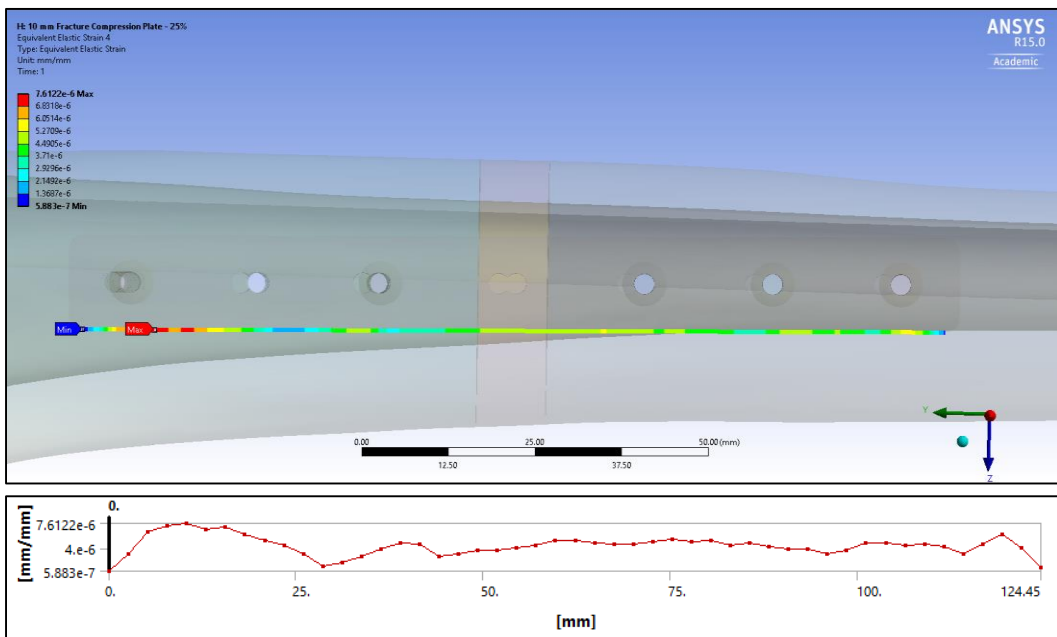


Figure B-4: 25% Callus stiffness – 400 N Compression – Plate side strain distribution.

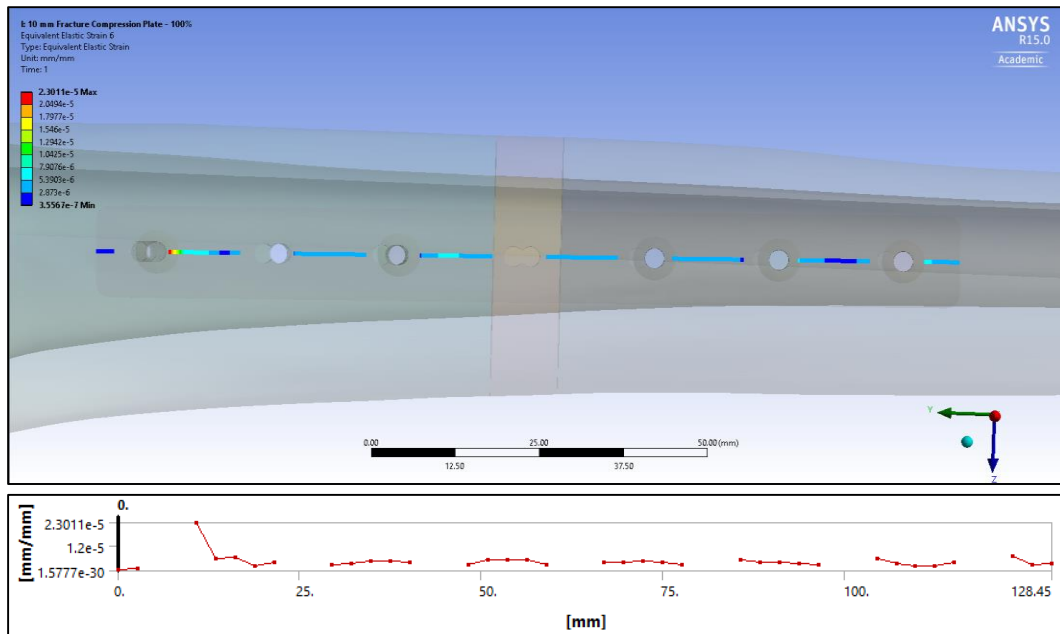


Figure B-5: 100% Callus stiffness – 400 N Compression – Plate center strain distribution.

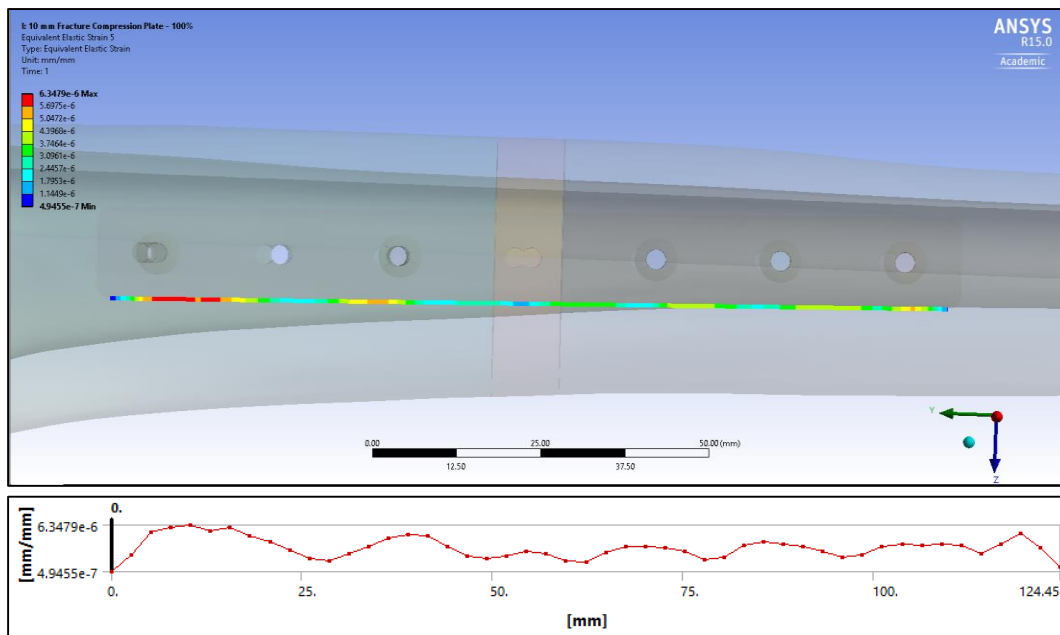


Figure B-6: 100% Callus stiffness – 400 N Compression – Plate side strain distribution.

REFERENCES

- [1] Buckwalter, J. a, Glimcher, M. J., Cooper, R. R., and Recker, R., 2009, "Bone Biology," pp. 1276–1289.
- [2] Carter, D. R., Van Der Meulen, M. C., and Beaupré, G. S., 1996, "Mechanical factors in bone growth and development.," *Bone*, **18**(1 Suppl), p. 5S–10S.
- [3] Keller, T. S., and Spengler, D. M., 1991, "Predicting the mechanical behavior of bone," *J. Biomech.*, **24**(9), p. 453.
- [4] Buckwalter, J. a, Glimcher, M. J., Cooper, R. R., and Recker, R., 1995, "Bone Biology," *J. Bone Jt. Surg.*, **77**(8), pp. 1276–1289.
- [5] Kumar, G., and Narayan, B., 2014, "The biology of fracture healing in long bones," *Class. Pap. Orthop.*, pp. 531–533.
- [6] Hak, D. J., Fitzpatrick, D., Bishop, J. A., Marsh, J. L., Tilp, S., Schnettler, R., Simpson, H., and Alt, V., 2014, "Delayed union and nonunions: Epidemiology, clinical issues, and financial aspects," *Injury*, **45**(SUPPL. 2), pp. S3–S7.
- [7] Stoffel, K., Klaue, K., Perren, S. M., Baumgart, F., and Fengels, I., 2001, "Functional load of plates in fracture fixation in vivo and its correlate in bone healing," *Injury*, **32**(SUPPL. 2), pp. 37–50+73.
- [8] Grasa, J., Gómez-Benito, M. J., González-Torres, L. a., Asiaín, D., Quero, F., and García-Aznar, J. M., 2010, "Monitoring in vivo load transmission through an external fixator," *Ann. Biomed. Eng.*, **38**(3), pp. 605–612.
- [9] Stephan, M., 2007, "Internal Fixation of Long Bone Fractures : the Scientific Basis of Biological Internal Fixation :," **84**(November 2002), pp. 1–24.
- [10] Wade, R., and Richardson, J., 2001, "Outcome in fracture healing: A review," *Injury*, **32**(2), pp. 109–114.
- [11] K-s, S., Piyaskulkaew, C., Chuntarapas, T., Jm, B., Hj, K., Ms, P., Kang, H., and Kd, R., 2014, "Dynamic Radiographic Criteria for Detecting," pp. 557–563.
- [12] Nakatsuchi, Y., Tsuchikane, A., and Nomura, A., 1996, "The vibrational mode of the tibia and assessment of bone union in experimental fracture healing using the impulse response method," *Med. Eng. Phys.*, **18**(7), pp. 575–583.
- [13] Richardson, J. B., Cunningham, J. L., Goodship, a E., O'Connor, B. T., and Kenwright, J., 1994, "Measuring stiffness can define healing of tibial fractures.," *J. Bone Joint Surg. Br.*, **76**(3), pp. 389–394.

- [14] Bourgois, R., and Burny, F., 1972, "Measurement of the stiffness of fracture callus in vivo. A theoretical study.," *J. Biomech.*, **5**(1), pp. 85–91.
- [15] Evans, M., Kenwright, J., and Cunningham, J. L., 1988, "Design and performance of a fracture monitoring transducer," *J. Biomed. Eng.*, **10**(1), pp. 64–69.
- [16] Ledet, E. H., D’Lima, D., Westerhoff, P., Szivek, J. A., Wachs, R. A., and Bergmann, G., 2012, "Implantable Sensor Technology: From Research to Clinical Practice," *J. Am. Acad. Orthop. Surg.*, **20**(6).
- [17] Muller, R., and Rueggsegger, P., 1995, "Three-dimensional finite element modelling of non-invasively assessed trabecular bone structures," *Med. Eng. Phys.*, **17**(2), pp. 126–133.
- [18] Dalstra, M., Huiskes, R., and van Erning, L., 1995, "Development and validation of a three-dimensional finite element model of the pelvic bone.," *J. Biomech. Eng.*, **117**(3), pp. 272–278.
- [19] Steiner, M., Claes, L., Ignatius, A., Simon, U., and Wehner, T., 2014, "Numerical simulation of callus healing for optimization of fracture fixation stiffness," *PLoS One*, **9**(7), pp. 1–11.
- [20] Ravikumar, N., 2015, "Development and Validation of an Optically-Based Strain Measuring Orthopedic Screw for Fracture Fixation Implants," Clemson University.
- [21] Kabel, J., Van Rietbergen, B., Odgaard, A., and Huiskes, R., 1999, "Constitutive relationships of fabric, density, and elastic properties in cancellous bone architecture," *Bone*, **25**(4), pp. 481–486.
- [22] Gaynor, E., 2014, "The mechanical properties of bone," *Clin. Orthop. Relat. Res.*, pp. 37–48.
- [23] Kemper, A., McNally, C., Kennedy, E., Manoogian, S., Tech, V., Forest, W., and Biomechanics, I., 2008, "The material properties of human tibia cortical bone," *Biomed. Sci. Instrum.*, **44**(1976), pp. 419–427.
- [24] Hölzer, J., Kampen, I., and Kwade, A., 1968, "Studies on the mechanical properties of single microorganisms," **61**(September), pp. 3–6.
- [25] Floerkemeier, T., Hurschler, C., Witte, F., Wellmann, M., Thorey, F., Vogt, U., and Windhagen, H., 2005, "Comparison of various types of stiffness as predictors of the load-bearing capacity of callus tissue.," *J. Bone Joint Surg. Br.*, **87**(12), pp. 1694–1699.
- [26] Burny, F., Donkerwolcke, M., Bourgois, R., Domb, M., and Saric, O., 1984,

“Twenty Years Experience in Fracture Healing Measurement with Strain Gauges,” *Orthopedics*, **7**(12), pp. 1823–1826.

- [27] Augat, P., Simon, Æ. U., Liedert, Æ. A., and Claes, Æ. L., 2005, “Mechanics and mechano-biology of fracture healing in normal and osteoporotic bone,” pp. 36–43.
- [28] Jagodzinski, M., and Krettek, C., 2007, “Effect of mechanical stability on fracture healing — an update,” *Injury*, **38**(1), pp. S3–S10.